NASA Technical Memorandum 4132

Attitude Angle Effects on Nimbus-7 Scanning Multichannel Microwave Radiometer Radiances and Geophysical Parameter Retrievals

Daniel S. MacMillan
ST Systems Corporation (STX)
Lanham, Maryland

Daesoo Han
Goddard Space Flight Center
Greenbelt, Maryland

National Aeronautics and
Space Administration
Office of Management
Scientific and Technical
Information Division

1989

TABLE OF CONTENTS

SECTION 1

INTRODUCTION

The Scanning Multichannel Microwave Radiometer (SMMR) on the Nimbus-7 spacecraft measures microwave radiances from the earth's surface and its surrounding atmosphere at five frequencies (6.6 GHz, 10.7 GHz, 18 GHz, 21 GHz, and 37 GHz) in both the horizontal and the vertical polarizations. A description of the SMMR instrument was given by Gloersen and Barath (1977). Radiances are collected with an offset parabolic reflector, which scans 25 degrees to the left and right of the satellite flight direction. The antenna beam scan lies along a conical surface with a 42-degree half angle from the nadir. The SMMR angle of incidence at the earth's surface is about 50.4 degrees when the spacecraft attitude angles vanish. However, there has been significant orbital and long-term variation of the spacecraft attitude. In this report, we examine the effect of this variation on SMMR radiances and retrievals.

In Section 2, we describe the actual attitude angle behavior of the Nimbus-7 SMMR in the long term, within an orbit, and within a scan. The effect of the attitude angle variation on the incident angle and on the polarization rotation angle is examined. In Section 3, the incident angle correction of SMMR radiances is discussed. First we look at the dependence of the sea surface emissivity on frequency, polarization, and the angle of incidence. Then a correction for a smooth ocean surface and no atmosphere is considered. To compensate for the incident angle variation, this correction was tested with SMMR radiance data. We then discuss the limitations of this simple correction and the dependence of incident angle sensitivity on surface roughness and atmospheric opacity.

Although the incident angle variation is small, its impact on the retrieved geophysical parameters computed from the Nimbus Experiment "Team Algorithms" (Nimbus-7 SMMR PARM Tape User's Guide, 1985) is large. The ocean surface microwave emissivity is quite sensitive to incident angle variation near the nominal SMMR incident angle of about 50 degrees. We have estimated the retrieval sensitivities for a smooth ocean surface and no atmosphere. A 1-degree increase in the angle of incidence produces a 2.9°C increase in retrieved sea surface temperature and a 5.7 m/sec decrease in retrieved sea surface wind speed. A clear example of this effect occurred when the Nimbus-7 spacecraft was pitched downward by about 0.4 degree in January 1984. There was a sudden jump in the bias errors of SMMR retrievals of sea surface temperature and sea surface wind speed. We discuss the effects of incident angle variation on Nimbus-7 SMMR retrievals in Section 4. Then we study the effect on the retrievals of applying the incident angle correction to the radiances required in the retrieval algorithms. In Section 5, we summarize our results and the remaining problems that need to be studied.

SECTION 2

ATTITUDE BEHAVIOR OF THE NIMBUS-7 SMMR

Effects of Attitude Variations

Spacecraft attitude variations affect the SMMR radiances in several ways. In this section we consider the effects on the incident angle and the polarization rotation angle. (The earth location vector is also affected.) Approximate expressions for these effects are derived to understand their behavior.

Incident Angle

Spacecraft attitude variations will change the direction of the SMMR boresight vector and, therefore, the incident angle at which the SMMR views the surface of the earth. In the spacecraft-centered coordinate system shown in Figure 2.1, any vector is transformed by a rotation matrix, **R**, that describes the attitude variation. The SMMR boresight unit vector is

$$\mathbf{w} = (-\sin\theta_S\cos\phi, -\sin\theta_S\sin\phi, -\cos\theta_S), \quad (1)$$

where θ_S is nominally the scan-cone angle of 42 degrees and ϕ is the antenna scan angle, which varies between −25 and 25 degrees. Since the spacecraft rotation angles are small, the rotated boresight vector is approximately

$$\mathbf{w}' = \mathbf{R}\mathbf{w} \approx \mathbf{w} + \Omega \times \mathbf{w}, \quad (2)$$

where the vector $\Omega = (\Omega_{roll}, \Omega_{pitch}, \Omega_{yaw})$. After rotation, the new angle, θ'_S, between $\mathbf{w}'$ and the z-axis is

$$\sin^2\theta'_S = |\mathbf{z} \times \mathbf{w}'|^2, \quad (3)$$

where **z** is the unit vector in the z-direction. To first order in the attitude angles,

$$\sin\theta'_S = \sin\theta_S[1 - (\Omega_{roll}w_2w_3 - \Omega_{pitch}w_1w_3)/\sin^2\theta_S]. \quad (4)$$

Using the above expression for the w_i, the change in θ_S from attitude rotation is

$$\delta\theta_S \approx \Omega_{pitch} \cos\phi - \Omega_{roll} \sin\phi. \quad (5)$$

If it is assumed that the earth is spherical and the satellite orbit is circular, then the incident angle $\psi = \beta + \theta_S$, where β is the angle between the vectors from the center of the earth to the subsatellite position and to the SMMR field of view. The variation of the incident angle away from the nominal angle of 50.4 degrees is

$$\delta\psi \approx F(\Omega_{pitch} \cos\phi - \Omega_{roll} \sin\phi). \quad (6)$$

The factor $F \approx 1.26$ is the geometric factor

$$F = 1 + (\sec^2\theta_S/\cos\beta)H(2R+H)/[2R(R+H)], \quad (7)$$

where H is the orbit height, R is the earth's radius, and β and θ_S are evaluated at their nominal values of 8.31 degrees and 42 degrees respectively.

Equation (6) shows that the orbital behavior of the incident angle arises from the orbital variation of the pitch; whereas, spacecraft roll angle determines most of the cross-track variation of the incident angle. From this expression, the incident-angle variation from +25 to −25 degrees across track is

$$\psi(-25) - \psi(+25) \approx 2\ F\ \Omega_{roll} \sin 25 = 1.06\ \Omega_{roll}. \quad (8)$$

We have examined the orbital behavior of the attitude angles with Grid-1 Antenna Temperature Tape (TAT) data from June 21, 1979 and October 25, 1979 by using the CELL tape generation program (User's Guide for the Nimbus-7 SMMR CELL-ALL Tape, 1988). For Grid-1, this program applies a radiometric calibration to the raw TAT data and remaps the data into a grid of five square cells across the orbital track. Attitude angles from the first (left) cell, third (center) cell, and fifth (right) cell were extracted. For June 21, 1979, values taken from the last three-fourths of orbit 3,315 and from the first one-fourth of orbit 3,316 form one complete set (orbit) of ascending node (AN) and descending node (DN) data. The same procedure was followed for orbits 3,321 and 3,322 (June 21, 1979) and orbits 5,056 and 5,057 (October 25, 1979). Figure 2.2 depicts AN and DN data from orbits 3,315-3,316 (June 21, 1979) and Figure 2.3 similarly shows the AN and DN values from orbits 3,321-3,322. The AN and DN data from October 25, 1979 is shown in Figure 2.4. The angles which define satellite attitude, that is, the pitch, roll, and yaw angles, are plotted in Figures 2.2-2.4 along with the incident angle minus the nominal incident angle of 50.4 degrees. The difference between the left and right cell incident angles was also plotted. This difference is a measure of the cross-track dependence of the incident angle.

Figures 2.2-2.4 show that the pitch and incident angle parallel each other so that the latitudinal variation of the incident angle is mostly dependent on the pitch. However, there is a contribution from spacecraft roll as scan angle increases away from the center position. This observation is consistent with equation (6) above. The incident angle is also dependent on scan position. This dependence is explicitly shown in the plots of the difference between left and right scan incident angles. These differences reach 0.8 degrees in some cases and are close to the roll angle in all of these figures. This observation agrees with equation (8) derived above for the cross-track variation. However, since the centers of the fifth and first Grid-1 cells are at scan angle of ±20 degrees, the cross-track incident angle variation here would be $2\ F\ \Omega_{roll} \sin 20 = 0.86\ \Omega_{roll}$.

Looking at Figures 2.2-2.4, one can see that there can be significant variation of the orbital behavior of the attitude angles within each operating day. In addition, there are differences between attitude angle variation in June and October 1979. One of the objectives of this examination is to demonstrate that the incident angle behavior was so variable that it will not be possible to make a systematic orbital correction of radiances. Instead, individual radiances need to be corrected with the attitude angles at the position of the radiance measurement. We will see in Section 3 that such a correction must also be highly dependent on the atmospheric and surface conditions of a particular radiance measurement.

Polarization Rotation

Attitude variations produce an additional rotation of the instrument feedhorn polarization axes with respect to the polarization axes corresponding to the surface in the look-direction. The coordinates of these axes are defined in Figure 2.1. To find this additional rotation angle, $\delta\phi$, we compute the rotated antenna vertical polarization vector, $\mathbf{v}' \approx \mathbf{v} + \Omega\times\mathbf{v}$, and the rotated boresight vector, $\mathbf{w}' \approx \mathbf{w} + \Omega\times\mathbf{w}$, where,

$$\mathbf{v} = (\cos\theta_S\cos\phi, \cos\theta_S\sin\phi, -\sin\theta_S), \quad (9)$$

and w is given by Equation (1). This rotation operation was described above in our discussion of the incident angle. We also need the surface horizontal polarization vector,

$$\mathbf{u}_S = \mathbf{w}' \times \mathbf{z} / \sin\theta_S, \quad (10)$$

where θ_S is the angle between $\mathbf{w}'$ and the z-axis. The rotation angle, $\delta\phi$, between $\mathbf{v}'$ and $\mathbf{v}_S$ is found from

$$\sin\delta\phi = \mathbf{v}'\cdot\mathbf{u}_S. \quad (11)$$

To first order in the attitude angle, this additional rotation angle is

$$\delta\phi \approx -(\Omega_{pitch}\sin\phi + \Omega_{roll}\cos\phi)/\sin\theta_S. \quad (12)$$

Njoku et al (1980) have given an equivalent expression for the Seasat SMMR.

The attitude angles typically vary between ±0.8 degree in each orbit. The yaw angle has little effect on $\delta\phi$ because yaw rotation is nominally about the vertical axis of the antenna horn and yields little change in the relative angle between the antenna polarization axes and the surface polarization axes. Figure 2.5 shows the polarization rotation angle, $\delta\phi$, from Equation (12) resulting from attitude variations in one orbit (seventh orbit on March 17, 1979). The rotation angle for the center ($\phi = 0$) and the ends ($\phi = \pm 25$ degrees) of the scan are shown in this figure. The cross-track variation of this angle comes from the pitch and is about 1.26 Ω_{pitch}.

One can make an estimate of the effect of an additional polarization rotation angle on the radiances. If there were no leakage between the horizontal and vertical polarization paths, then in terms of the actual radiances (H,V), the antenna temperatures would be

$$\begin{pmatrix} T_X \\ T_y \end{pmatrix} = \begin{pmatrix} \cos^2\phi & \sin^2\phi \\ \sin^2\phi & \cos^2\phi \end{pmatrix} \begin{pmatrix} H \\ V \end{pmatrix}. \quad (13)$$

Inverting this, one finds that the variation of the radiances with respect to scan angle is

$$\frac{\partial}{\partial\phi}\begin{pmatrix} H \\ V \end{pmatrix} = \begin{matrix} \sin 2\phi \\ \cos^2 2\phi \end{matrix} \begin{pmatrix} T_X - T_y \\ T_y - T_X \end{pmatrix}. \quad (14)$$

For typical 6.6 GHz antenna temperatures (T_X = 96 K and T_y = 135 K), the radiance sensitivity to a change in rotation angle at 25 degrees is

$$\begin{pmatrix} \Delta H \\ \Delta V \end{pmatrix} = -1.25 \text{ K/deg}. \quad (15)$$

Typical orbital attitude variations (Figure 2.5) produce variations of the rotation angle in Equation (12) of between −1 and +1 degree. This will have a considerable effect on the cross-track behavior of the radiances. For example, an additional polarization angle of 1 degree will yield a cross-track effect of 2.5 K.

Currently SMMR radiances are computed from antenna temperatures with polarization rotation angles (offset angles, $\delta\phi_X$ and $\delta\phi_y$) that are independent of scan angle (Gloersen et al., 1980). These offset angles are thought to originate from leakage in the polarization selector switches (Han and Kim, 1988). This means that, instead of Equation (13), we have used

$$\begin{pmatrix} T_X \\ T_y \end{pmatrix} = \begin{pmatrix} \cos^2(\phi + \delta\phi_X) & \sin^2(\phi + \delta\phi_X) \\ \sin^2(\phi + \delta\phi_y) & \cos^2(\phi + \delta\phi_y) \end{pmatrix} \begin{pmatrix} H \\ V \end{pmatrix}. \quad (16)$$

This form of the equation was proposed by Gloersen et al. (1980) and the offset angles were found by fitting the equation to measured data. One should also include the polarization rotation offset angle given by Equation (12) in this formulation.

Long-Term Behavior of SMMR Incident Angle

Over its lifetime, Nimbus-7 spacecraft has had significant variations of attitude. The long-term behavior of the resulting incident angle at the center scan position is shown in Figure 2.6 beginning in January 1979 (month 1). This behavior was found from monthly averages of the incident angle for ocean latitudes between 60°S and 60°N. In January 1984 (month 61), the spacecraft was pitched downward by 0.4 degrees. Consistent with Equation (6), this change produced a 0.5-degree decrease in the incident angle. However, one can see that the behavior of the incident angle was already changing by October 1982. Figure 2.6 also shows that the annual cycles of the day and night incident angles changed after 1983. Within an orbit, the incident angle varies by about one to two degrees depending on the year. The average night incident angle is less than the average day incident angle by about 0.2-0.3 degree. This difference can probably be attributed to the inaccuracy of attitude determination in the descending segment (nighttime) of each orbit when only the horizon sensors are used. In the next section, we describe the orbital behavior of the incident angle found from the spacecraft attitude angles. It will be evident that there was a discontinuous jump of about 0.2-0.3 degrees in the computed incident angle when the spacecraft passed into or out of view of the sun.

Orbital Behavior of the Incident Angle

We have investigated the dependence of incident angle on season, latitude, and scan position by using Grid-3 (13 cells across the orbital track) CELL data (C. C. Fu et al., 1988). For convenience, the incident angle was determined as a function of a spacecraft ecliptic angle, which is defined in the following way:

$$\begin{matrix} e = 90 - d_S + lat_S & \text{ascending node} \\ 270 - d_S - lat_S & \text{descending node,} \end{matrix} \quad (17)$$

where d_S is the solar declination angle, which varies from −23.5 degrees on December 22 to 23.5 degrees on June 22 and lat_S is the subsatellite latitude. Much of the seasonal variation should be removed by using this angle, because it accounts for seasonal changes in sun position.

The zonal means of the incident angle appear in Figures 2.7-2.20 for each January, April, July, and October from 1979 through 1985. The orbital incident angle range varied significantly over this period. For example, in January 1979 it was about 50.0 to 51.0 degrees and in April 1985, it was 49.2 to 50.5 degrees. The incident angle is generally greater in the southern hemisphere than in the northern hemisphere and the effect of scan position is greatest in the high latitudes. For both the AN and DN, the greatest incident angle values occur in the southern hemisphere at the right-scan position and in the northern hemisphere at the left-scan position. The incident angle at the right scan position has the greatest orbital variation.

As noted above, the global average incident angle behavior changed after July 1982. This change can also clearly be seen in the monthly average orbital incident angle plots. From January 1979 to July 1982, zonal incident angles varied little from one year to the next. However, after July 1982, the effect of scan position on incident angle is more noticeable. In January 1984, the Nimbus-7 satellite was pitched downward, thereby decreasing the incident angle by about one-half degree. Comparison of the incident angle behavior for January 1984 (Figure 2.17a) and January 1979 (Figure 2.7a) clearly indicates both the greater dependence on scan position in the later years of operation and the decrease in incident angle values between 1980 and 1984. The decrease in incident angle is evident for all latitudes.

For ecliptic angles between 210 and 330 degrees, a characteristic sharp drop of about 0.2 degrees in the incident angle can be seen until July 1984. This drop corresponds to the nighttime portion of the orbit, when the satellite only used horizon sensors to determine its orientation in space. The disappearance of this drop in the plots after July 1984 is caused by the fact that after August 21, 1984, daytime attitude determination also only used the horizon sensors without the sun sensor. Until January 1984, the incident angle curves at the three scan positions approximately intersected at an incident angle of 50.4-50.5 degrees in the AN and 0.2 degree less at 50.2-50.3 degrees in the DN. This AN intersection point nearly equals the nominal incident angle of 50.4 degrees. By Equation (6), these three curves can only intersect when the deviation, $\delta\psi$, of the incident angle from its nominal value vanishes. At such points, the pitch and roll angles must also be zero. Since the intersection point should correspond to the nominal incident angle, the error in the nighttime incident angle must be −0.2 degree. After the spacecraft was pitched downward by 0.4 degree in January 1984, there was a dramatic change in the orbital behavior of the incident angle. The intersection points dropped by 0.4-0.5 degrees to 50.0 degrees in the AN and 49.8 degrees in the DN and then continued to decrease by another 0.2 degree through October 1985.

SECTION 3

RADIANCE DEPENDENCE ON INCIDENT ANGLE

Average Incident Angle Correction of Radiances

Even incident angle variations of less than 1 degree have a large effect on geophysical retrievals (Han et al., 1987). This is because measured microwave radiances are so sensitive to changes in the incident angle. To simplify our calculation, we have estimated this dependence by using the sensitivity for a specular sea surface of temperature 20°C and no atmosphere. In this case the incident angle sensitivity is

$$\partial T_B/\partial\psi = T_S\,\partial\varepsilon_o/\partial\psi, \qquad (18)$$

where T_S is the sea surface temperature (SST) fixed at 20°C and ε_o is the smooth surface emissivity. The ocean surface emissivities were computed from the Fresnel reflection coefficients for horizontal and vertical polarization. An expression for the sea water dielectric constant was taken from Chang and Wilheit (1979), and a salinity of 35 °/oo was used. Figure 3.1 shows the resulting radiances at three of the five SMMR frequencies as a function of the angle of incidence. The derivatives of these radiances with respect to the angle of incidence at 50 degrees are given in Table 1. This sensitivity is about −1.5 K/degree for the horizontal channels and 2.2 K/degree for the vertical channels.

Correction of Global Average Ocean Radiances

To account for incident angle variation, we adjusted the brightness temperatures with the incident angle sensitivities for a smooth ocean surface and clear atmosphere. The corrected brightness temperatures are given by

$$T_B(\text{corrected}) = T_B(\text{uncorrected}) - \alpha(\psi - \psi_o), \qquad (19)$$

where ψ is the incident angle, ψ_o is the nominal SMMR incident angle (50.4 degrees), and $\alpha = \delta T_B/\delta\psi$ from

Equation (18) is taken from Table 1. This correction adjusts the radiances to radiances at the nominal incident angle. In Figures 3.2-3.11, we show the long-term global average behavior of the nighttime and daytime SMMR radiances before and after the correction. The downward trend in the vertical channels beginning in 1984 is removed. The correction tends on average to over correct the horizontal radiances especially at the higher frequencies. In the next section, we will examine the results of this simple correction and the dependence of the radiances on incident angle in more detail.

The correction appears to remove the long-term trends of the nighttime radiances better than for the daytime radiances. After August, 1984 (month 68), the daytime radiances have been overcorrected. The reason for this is that the incident angle used for the correction in Equation (19) is too small by 0.2 degrees for the daytime portion of each orbit after August 21, 1984. As noted in Section 2, this is because only the horizon sensors were employed for attitude determination after this date. By Table 1, the daytime radiances after August 21, 1984 should be adjusted by -0.43 K for the vertical polarization and by 0.28 K for the horizontal polarization.

Model Calculation of Incident Angle Sensitivity

The incident angle sensitivity of the radiances depends on the surface roughness and atmospheric opacity. We have studied this sensitivity using the brightness temperature model of Chang and Wilheit (1979). For fixed wind speed and SST (285 K), the model was run for 81 different combinations of 9 atmosphere types and 9 cloud models. Figures 3.12-3.16 show the radiance sensitivities to incident angle as a function of radiance for eight wind speed choices (0, 5, 10,...,25 m/sec). Each set of points corresponding to a fixed wind speed shows the effect of atmospheric opacity on incident angle sensitivity. As a function of wind speed, these model brightness temperatures increase faster than the actually observed SMMR brightness temperatures because the wind speed dependence of the model is not correct.

To understand why these sensitivity curves have this form, it is instructive to consider the isothermal atmosphere model. If the atmosphere is isothermal, then the radiances are

$$T_B = T_S[1 - (1 - \varepsilon)\, e^{-2\tau}] + T_{sp}(1 - \varepsilon)\, e^{-2\tau}, \qquad (20)$$

where $\tau = \tau_0/\cos\psi$, τ_0 is the vertical atmospheric opacity, and T_{sp} is the 2.7 K cosmic background temperature. Here, ε is the rough surface emissivity. The sensitivity with respect to the angle of incidence is

$$\partial T_B/\partial\psi = (T_S - T_{sp})e^{-2\tau}[\partial\varepsilon/\partial\psi + 2\tau\,(1 - \varepsilon)\tan\psi]. \qquad (21)$$

This sensitivity depends upon the incident angle sensitivities of both the surface emissivity and the atmospheric path length. For fixed surface conditions (wind speed and SST), the overall sensitivity depends only on τ, which is approximately linear in T_B. For reference, we have also shown in Figures 3.12-3.16 the sensitivity in Equation (21) for the isothermal atmosphere case with the surface wind speed set to zero (solid line). The simple correction in Equation (18) corresponds to the leftmost point of the isothermal curve where the opacity, τ, is zero. The differences between the isothermal case and the nonisothermal model arise from upwelling and downwelling radiation terms.

Figures 3.12-3.16 show that the vertical channel sensitivities are much less dependent on atmospheric opacity and surface wind speed than are the horizontal channel sensitivities. This is expected because, near a 50-degree incident angle, the horizontal radiances are much more dependent on windspeed than are the vertical channels (Stogryn, 1967). As a function of atmospheric opacity, the incident angle sensitivity also varies much less for the vertical channels than for the horizontal channels. This can be seen for the isothermal atmosphere case of Equation (18) in which the derivatives of the horizontal and vertical emissivities have opposite signs.

The correction in Equation (19) may be sufficient to correct the global average radiances if α is adjusted for global average atmospheric and surface conditions. It may not even be necessary to correct the global average horizontal radiances (especially at the higher frequencies), because the incident angle sensitivity has such a wide variation over different atmospheric and surface conditions. However, for individual retrievals, the incident angle sensitivity must reflect the specific local atmospheric and surface conditions. We can see that, in order to correct the actual radiances to the radiances at the nominal (50.4 degrees) incident angle, we need to compute the incident angle sensitivity. However, this sensitivity depends on the surface conditions and the atmospheric opacity, which are the quantities that we are trying to retrieve. An iterative procedure might be employed in the retrieval whereby the radiances are corrected with the retrieved wind speed and the wind speed is recomputed with the corrected radiances. In addition, one would need a surface emissivity model that adequately describes the surface roughness, foam effects, and incident angle dependence.

INCIDENT ANGLE EFFECT ON SMMR RETRIEVALS

Retrieval Sensitivities to Incident Angle

Sea surface wind speed, sea surface temperature (SST), and atmospheric water vapor content are three of the geophysical parameters that are derived from SMMR radiances. Table 1 gives the sensitivities of the Nimbus Experiment "Team Algorithms" to radiance variations of 1 K. These sensitivities were evaluated for typical average global ocean radiances. When these sensitivities are multiplied by the brightness temperature sensitivities to incident angle, the retrieval algorithm sensitivities to incident angle change shown in Table 1 result. A 1-degree increase in incident angle yields an increase of 2.9°C in retrieved SST, a decrease of 5.7 m/sec in retrieved windspeed, and only a 0.15 cm increase in water vapor content. In the rest of this section, we show the results of applying the simple approximate correction in Equation (19) to the SMMR radiances before putting them into the geophysical retrieval algorithms.

SST Retrievals

We have computed the monthly average differences between retrieved SST and a climatological SST. The retrieval algorithm used is a prelaunch version, Basic Version 1 (Nimbus-7 SMMR PARM User's Guide, 1985), with only an initial tuning. The SST difference is plotted with and without incident angle correction in Figure 4.1. There is a long-term downward trend in both cases caused mainly by a corresponding downward trend in the 6.6 GHz vertical brightness temperature, which is the principal surface channel for SST retrieval. The decrease in the SST difference before October 1983 (month 58) reflects the behavior of the 21 GHz horizontal channel. The long-term drift behavior of this channel changed after May 1983. The additional decrease in Figure 4.1a between 1983 and 1984 is caused by the incident angle decrease. According to Table 1, a 0.5 degree decrease in the incident angle produces a decrease of about 1.5°C in retrieved SST. This decrease occurs despite the presence of an explicit incident angle dependence of −3°C/deg in the algorithm. In Figure 4.1b, we can see a clear improvement in the corrected SST retrievals after 1983. The remaining drift is due to the drifts of the 6.6 GHz and 10.7 GHz radiances in Figures 3.2-3.5. With the algorithm sensitivities from Table 1, these radiance drifts yield an SST drift of −1°C, which is approximately what is shown in Figure 4.1b.

We have also examined the incident angle effect on a second SST retrieval algorithm, Basic Version 2 (Nimbus-7 SMMR PARM User's Guide, 1985), which does not use 21 GHz radiances. Figure 4.2 shows both uncorrected and corrected monthly SST anomalies from 1979 to 1984. During 1984, there was a sharp downward trend caused by the corresponding decrease in incident angle, which is effectively removed by the correction. The unusually low dip during the latter half of 1983 shown in Figure 4.1 (Basic Version 1) does not appear for Basic Version 2. This indicates that the dip is due to the abnormal behavior of the 21 GHz horizontal radiance. The remaining drift for Version 2 is caused by the downward drift of the 6.6 GHz vertical radiance.

Wind Speed Retrievals

Coincident wind speed observations from ships and from SMMR have been compared for the period January 1979 to December 1984. The average monthly differences of these coincident observations are shown in Figure 4.3a. It is clear that the decrease in incident angle between 1983 and 1984 produced the observed increase in retrieved wind speeds of about 3-4 m/sec. This is because a 0.5 degree decrease in incident angle causes an increase in retrieved wind speed of about 2.9 m/sec.

The wind speed retrieval comparisons after making the radiance correction in Equation (19) are shown in Figure 4.3b. Without correction, daytime differences in wind speed were greater than nighttime differences. We noted in Section 2 that the nighttime incident angles are systematically lower than the daytime incident angles by about 0.2 degree. Therefore, 0.2 degree was added to the nighttime incident angles when wind speed retrievals were corrected. It can be seen that this adjustment reduced the difference between the day and night wind speed bias errors. However, after August 21, 1984 (month 68), the daytime differences should also be adjusted to account for the fact that daytime incident angles after this date are also systematically 0.2 degree too low (Section 2). Using the windspeed retrieval algorithm sensitivity to incident angle from Table 1, these windspeed differences should be adjusted upward by 1.14 m/sec.

We can see a clear improvement in wind speed retrievals after 1983. The large jump in bias error of the retrieved windspeed is removed by the correction. However, the sensitivities of the correction may need to be adjusted to reflect surface and atmospheric conditions.

SECTION 5

SUMMARY OF RESULTS

SECTION 5

SUMMARY OF RESULTS

Incident angle behavior in the short term and long term have been analyzed. We have examined the radiance dependence on incident angle and have applied a simple correction to account for incident angle variation. Most of the incident angle effects in the SST and surface-wind speed retrievals are removed when this correction is applied to the radiances. One of the problems with this simple correction is that the incident angle sensitivity depends on the surface conditions and atmospheric opacity. These are quantities that we are trying to retrieve. It may be possible to use an iterative method in which the radiances are computed with initial retrievals and then the retrievals are recomputed with the corrected radiances. One should also use an ocean surface emissivity model that adequately describes the surface roughness, foam effects, and incident angle dependence. Another problem that needs to be considered is the uncertainty in spacecraft attitude information. For instance, it was observed that the incident angle, derived from spacecraft attitude angles, is systematically about 0.2 degree low when only horizon sensors were used for attitude determination (nighttime and then also daytime after August 21, 1984).

SECTION 6

REFERENCES

Chang, A. T. C., and T. T. Wilheit, Remote sensing of atmospheric water vapor, liquid water, and wind speed at the ocean surface by passive microwave techniques from the Nimbus-5 Satellite, *Radio Sci., 14*, 793-802, 1979.

Fu, C. C., D. Han, S. T. Kim, and P. Gloersen, *User's guide for the Nimbus-7 Scanning Multichannel Microwave Radiometer (SMMR) CELL-ALL tape*, NASA Reference Publication 1210, October 1988.

Gloersen, P., and F. T. Barath, A Scanning Multichannel Microwave Radiometer for Nimbus-G and Seasat-A, *IEEE J. Oceanic Eng., OE-2*, 172-178, 1977.

Gloersen, P., D. J. Cavalieri, and H. V. Soule, An alternative algorithm for correction of the Scanning Multichannel Microwave Radiometer polarization radiances using Nimbus-7 observed data, NASA Technical Memorandum 80672, 1980.

Han, D. and S. T. Kim, Effects of switch leakages upon Nimbus-7 SMMR calibration, NASA Technical Memorandum, 1988.

Han, D., D. MacMillan, S. T. Kim, and C. C. Fu, Incident angle effect on geophysical parameter retrieval from the Nimbus-7 SMMR, International Workshop on Remote Sensing Retrieval Methods, Williamsburg, Virginia, 1987.

Nimbus-7 Scanning Multichannel Microwave Radiometer (SMMR) PARM Tape User's Guide, NASA Goddard Space Flight Center, Greenbelt, MD, 1985.

Njoku, E. G., E. J. Christensen, and R. E. Colfield, The Seasat Scanning Multichannel Microwave Radiometer (SMMR): antenna pattern corrections-development and implementation, *IEEE J. Oceanic Eng., OE-5*, 125-137, 1980.

Stogryn, A., The apparent temperature of the sea at microwave frequencies, *IEEE Trans. on Antennas and Propagation, AP-15*, 278-286, 1967.

TABLE 1

Retrieval Sensitivities to Change in the Angle of Incidence
(smooth surface and no atmosphere)

			SST	Wind Speed		Water Vapor	
Channel	$\frac{\partial T_B}{\partial \psi}$	$\frac{\partial SST}{\partial T_B}$	$\frac{\partial SST}{\partial \psi}$	$\frac{\partial W}{\partial T_B}$	$\frac{\partial W}{\partial \psi}$	$\frac{\partial WV}{\partial T_B}$	$\frac{\partial WV}{\partial \psi}$
	$\frac{K}{deg}$	$\frac{°C}{K}$	$\frac{°C}{deg}$	$\frac{m/sec}{K}$	$\frac{m/sec}{deg}$	$\frac{cm}{K}$	$\frac{cm}{deg}$
6.6H	-1.3	-0.37	0.48	-	-	-	-
6.6V	2.1	1.70	3.57	-	-	-	-
10.7H	-1.3	-0.44	0.57	1.81	-2.35	-	-
10.7V	2.1	0.65	1.37	-0.86	-1.81	-	-
18H	-1.4	-0.17	0.24	-	-	-0.05	0.07
18V	2.1	-0.10	-0.21	-	-	-0.02	-0.04
21H	-1.5	0.10	-0.15	-	-	0.06	-0.09
21V	2.2	-	-	-	-	0.05	0.10
37H	-1.6	-	-	0.13	-0.21	-0.03	0.04
37V	2.2	-	-	-0.60	-1.32	0.03	0.07
TOTAL EFFECT			2.87*		-5.69		0.15

* Includes an explicit algorithm dependence of -3ψ.

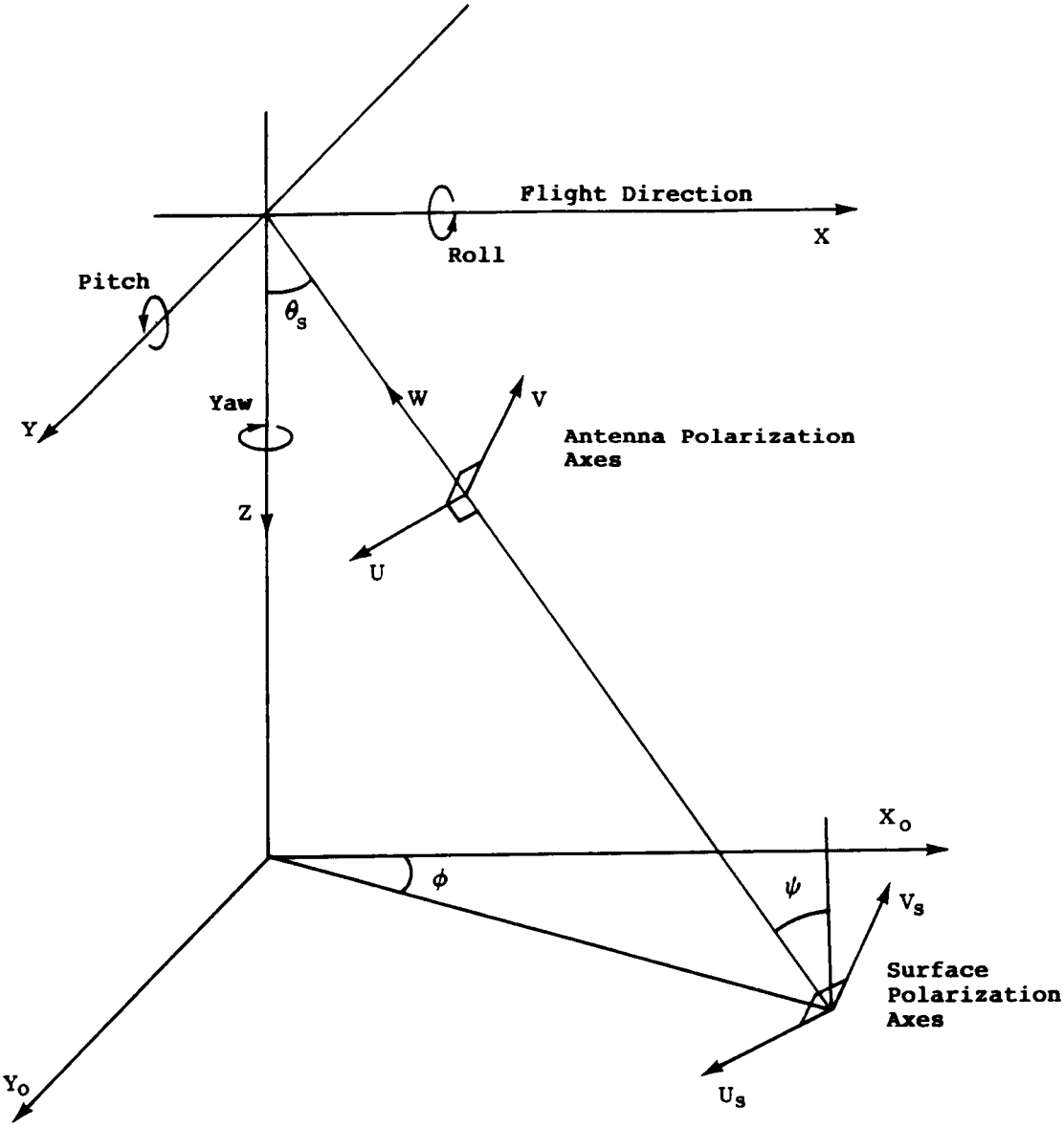

Figure 2.1 The antenna polarization axes and the surface polarization axes in the spacecraft-centered coordinate system. The scan angle is ϕ, the angle between the boresight and the nadir is θ_s (nominally equal to the half-cone angle of 42 degrees), and the incident angle ψ is nominally 50.4 degrees.

(a)

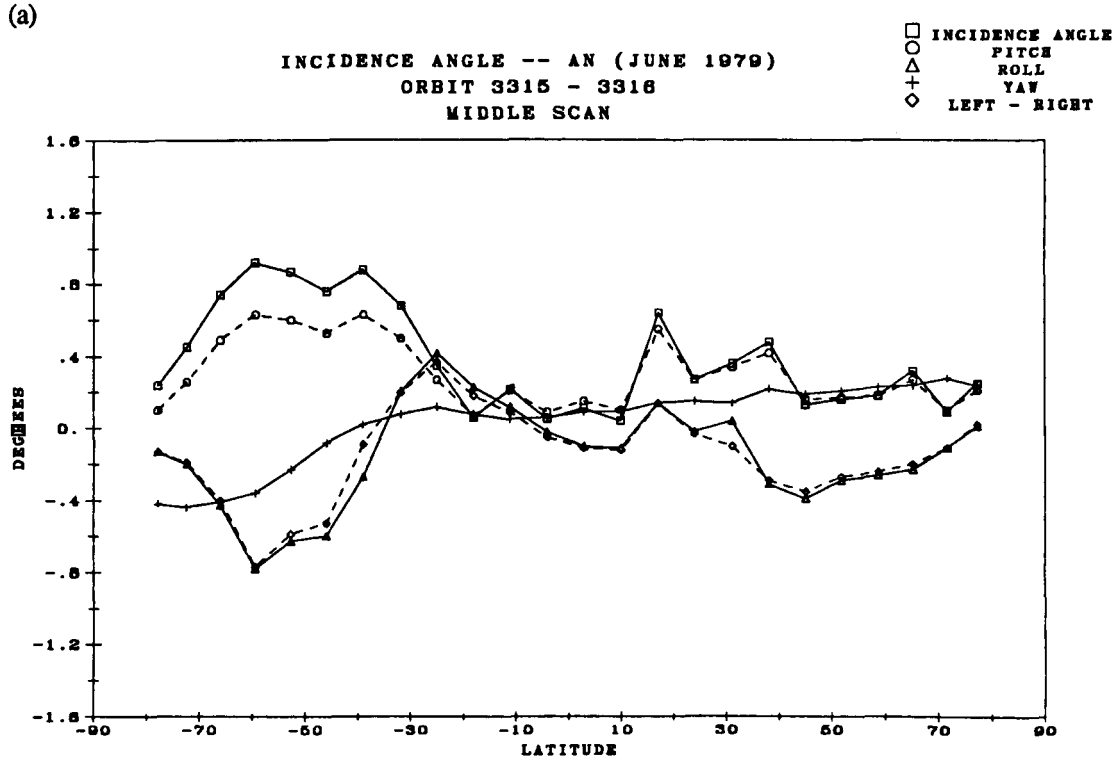

(b)

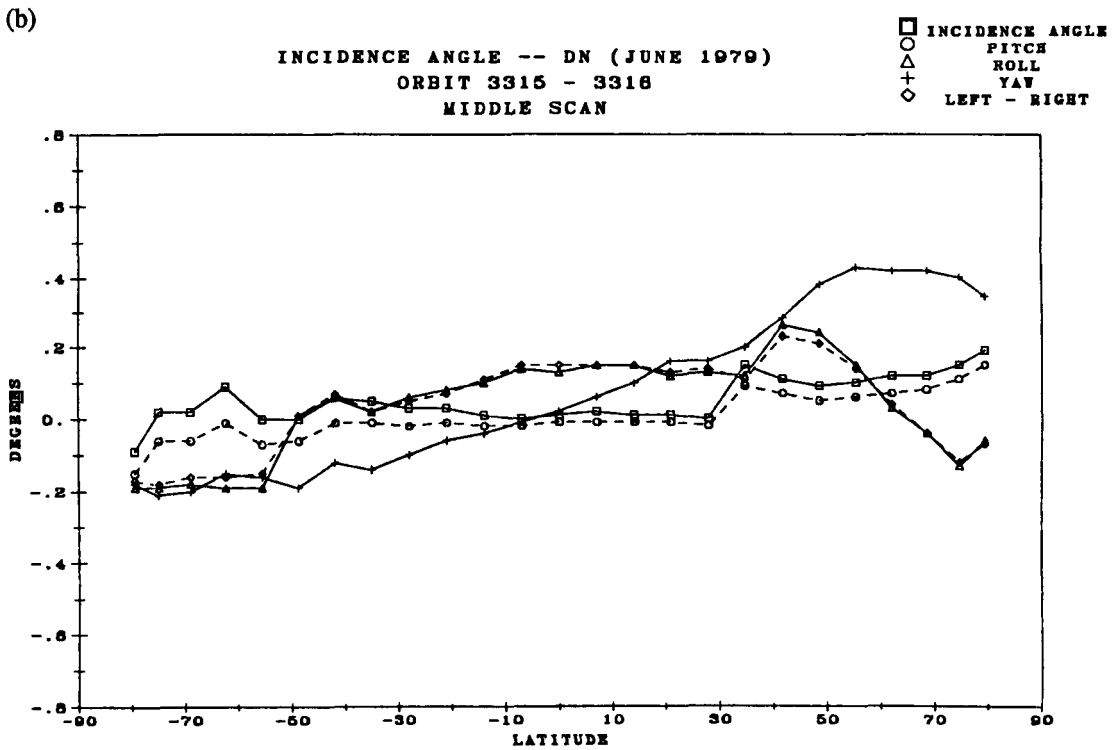

Figure 2.2 Incident angle and attitude angles at the middle scan position and the difference between the left and right scan position incident angles for the ascending node (a) and descending node (b) of orbits 3315 and 3316 in June 1979.

(a)

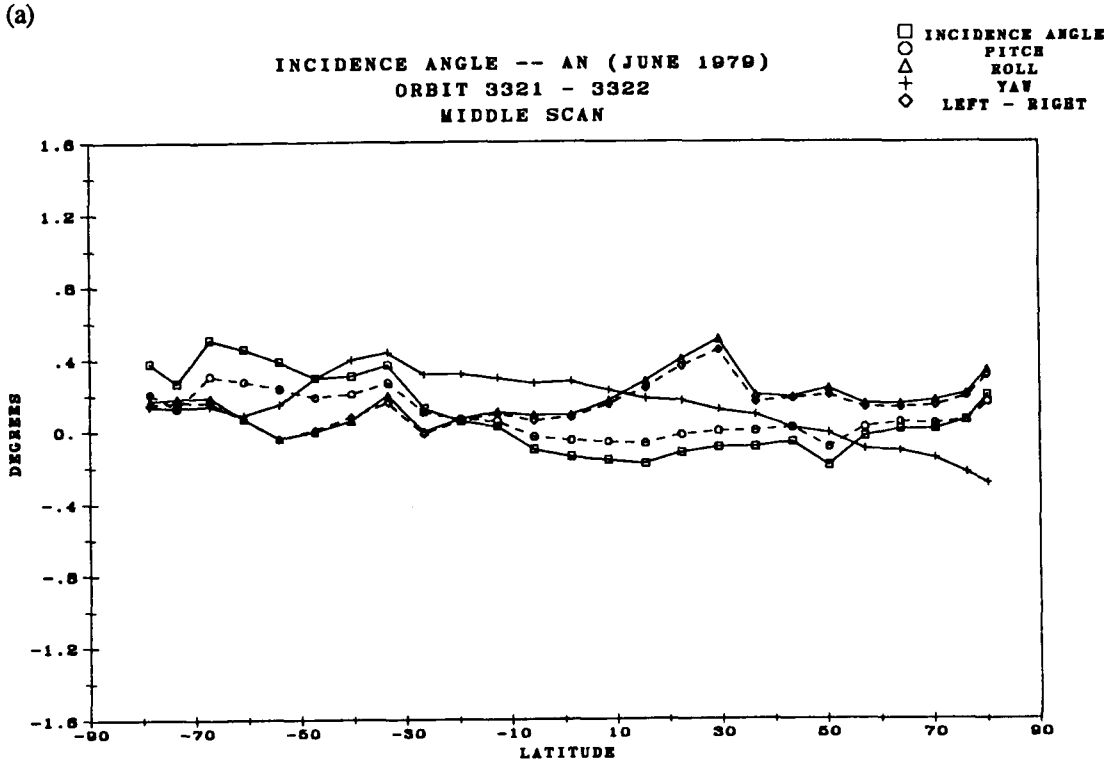

(b)

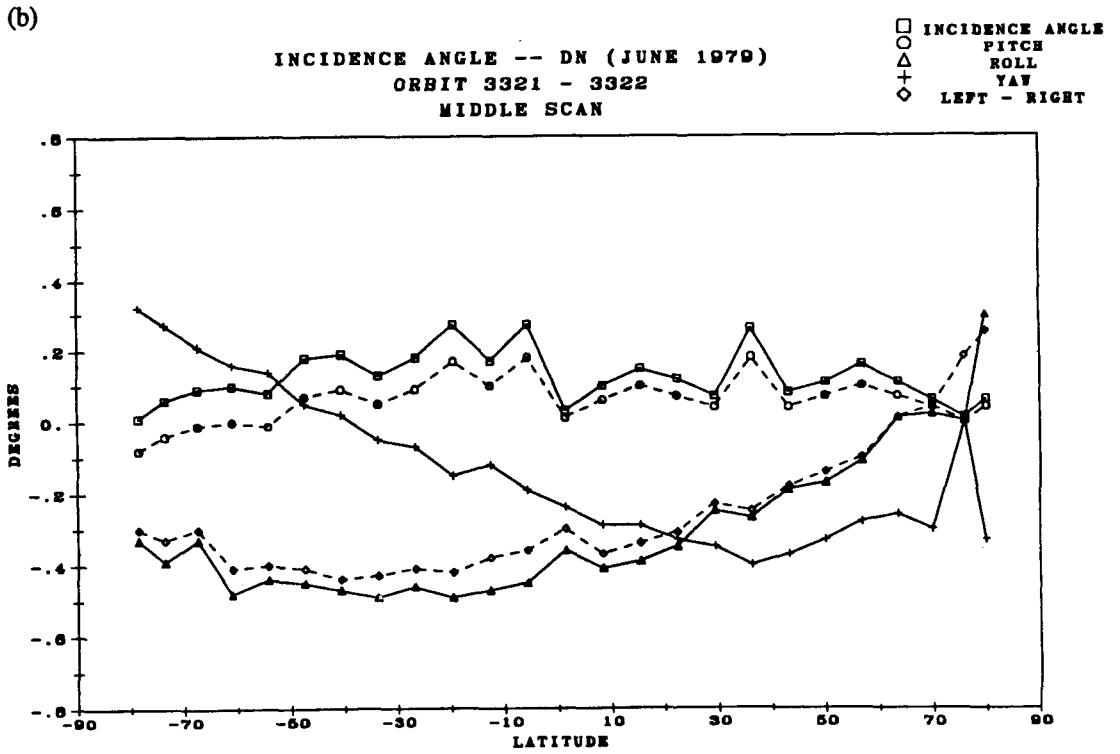

Figure 2.3 Incident angle and attitude angles at the middle scan position and the difference between the left and right scan position incident angles for the ascending node (a) and the descending node (b) of orbits 3321 and 3322 in June 1979.

(a)

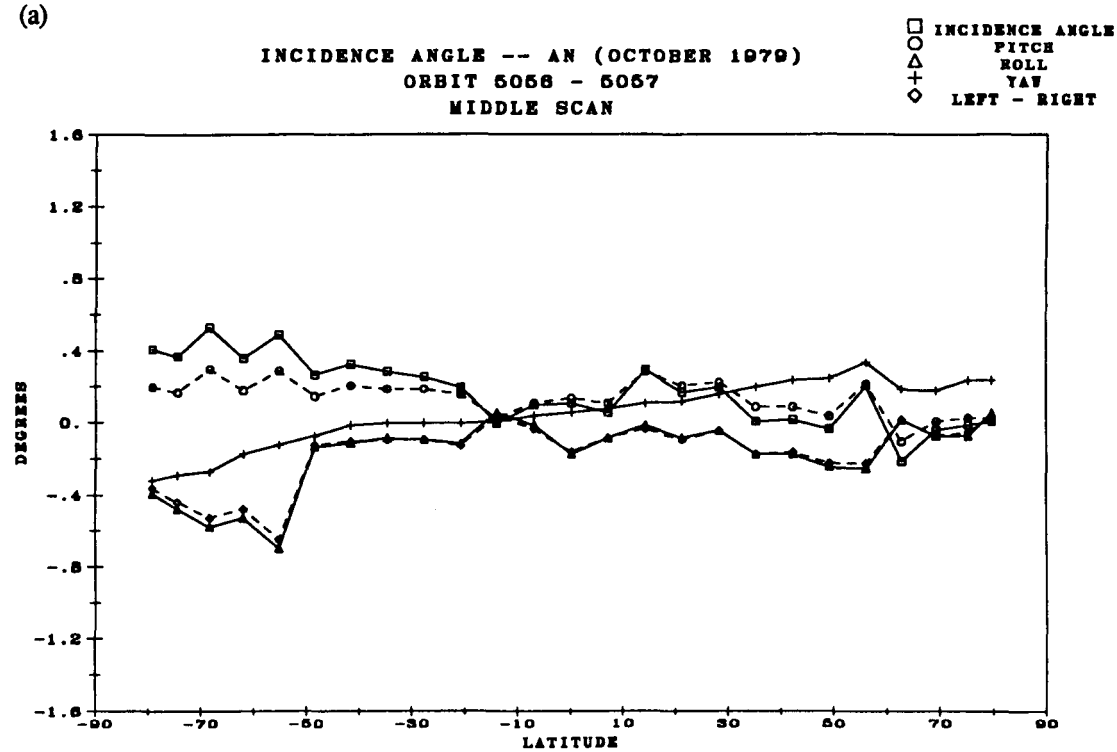

(b)

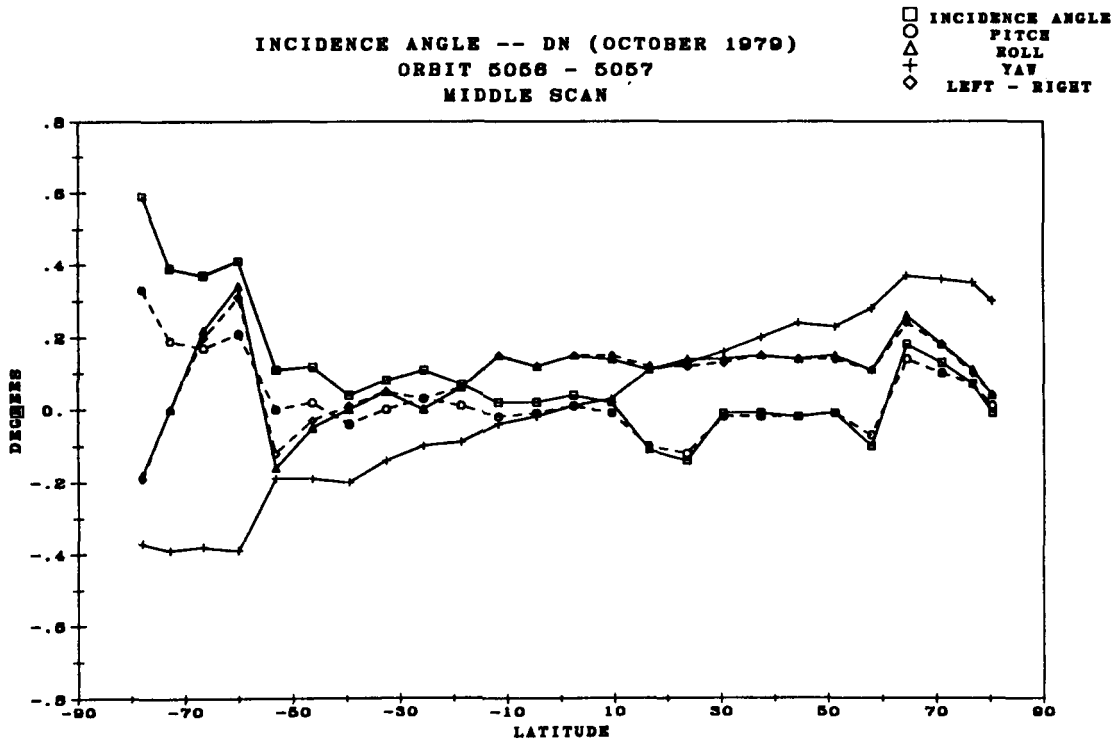

Figure 2.4 Incident angle and attitude angles at the middle scan position and the difference between the left and right scan position incident angles for the ascending node (a) and descending node (b) of orbits 5056 and 5057 in October 1979.

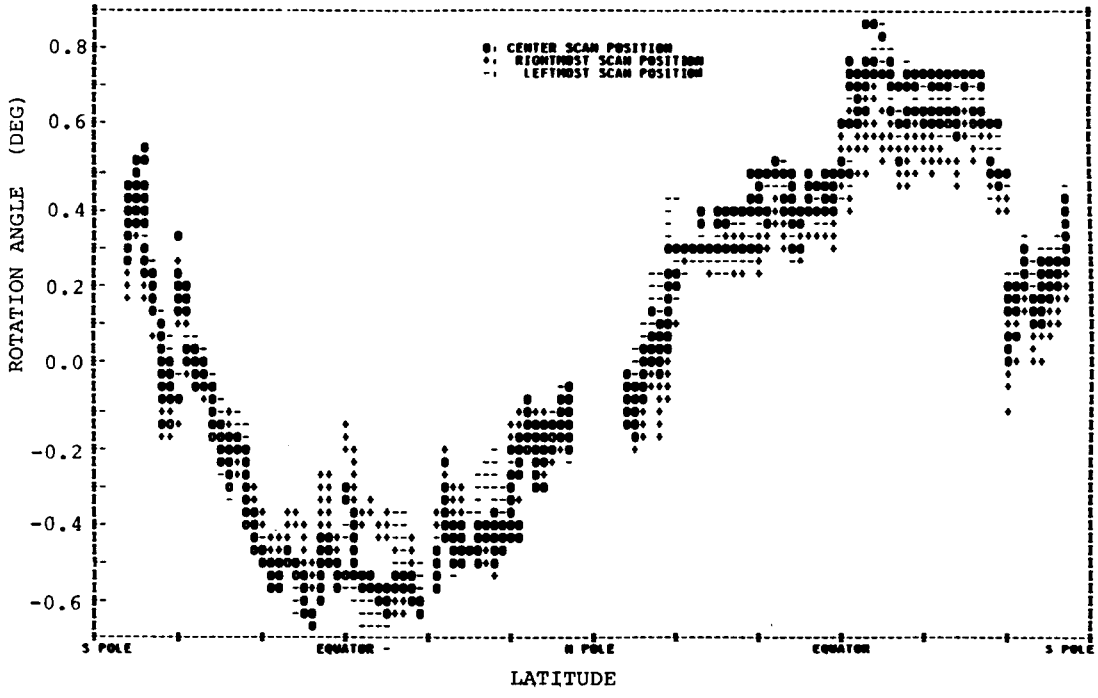

Figure 2.5 Polarization rotation angle from orbital attitude variation of the seventh orbit from March 17, 1979.

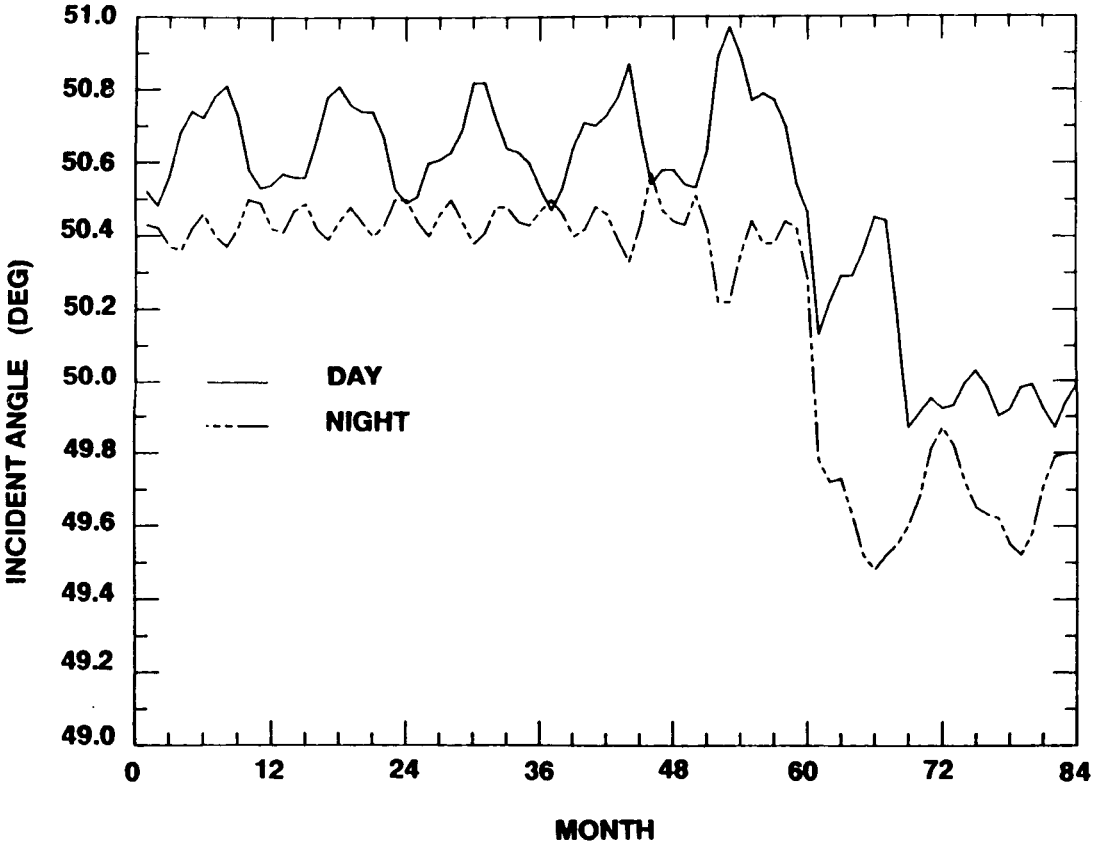

Figure 2.6 Monthly average SMMR incident angle for ocean latitudes between 60 deg S and 60 deg N.

(a)

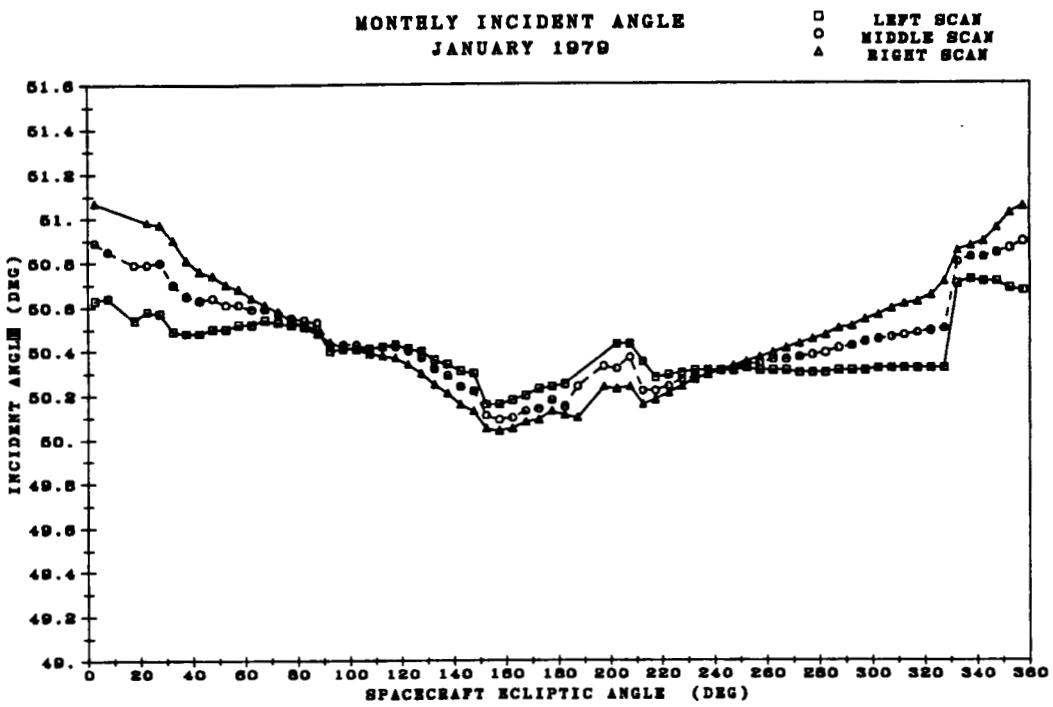

(b)

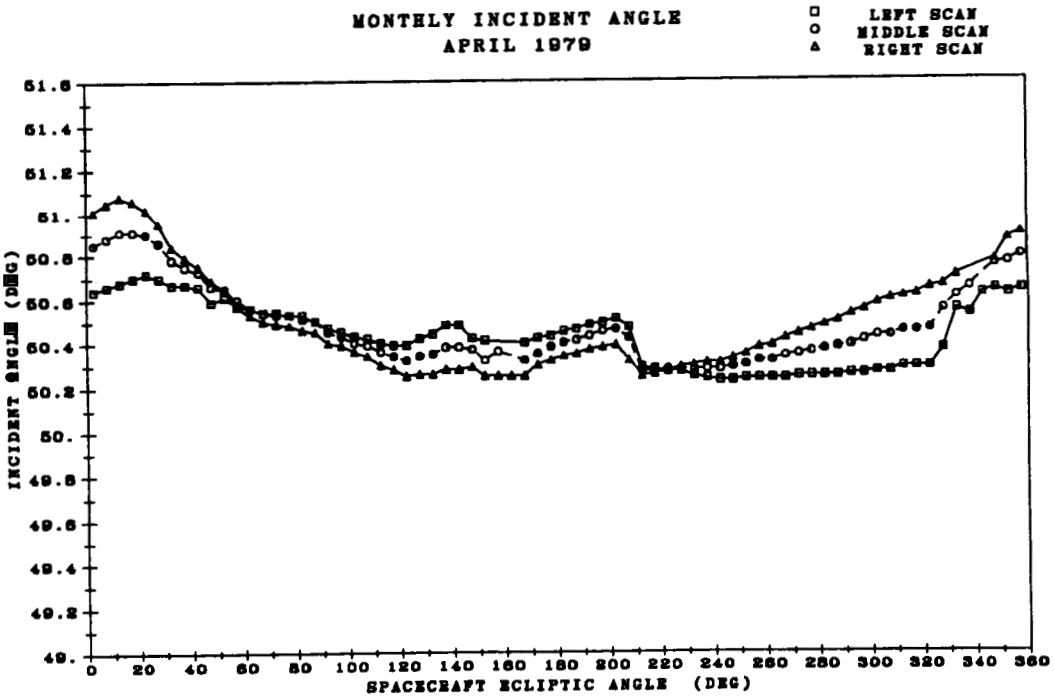

Figure 2.7 Monthly average incident angle in January 1979 (a) and April 1979 (b) for three scan positions as a function of spacecraft ecliptic angle.

(a)

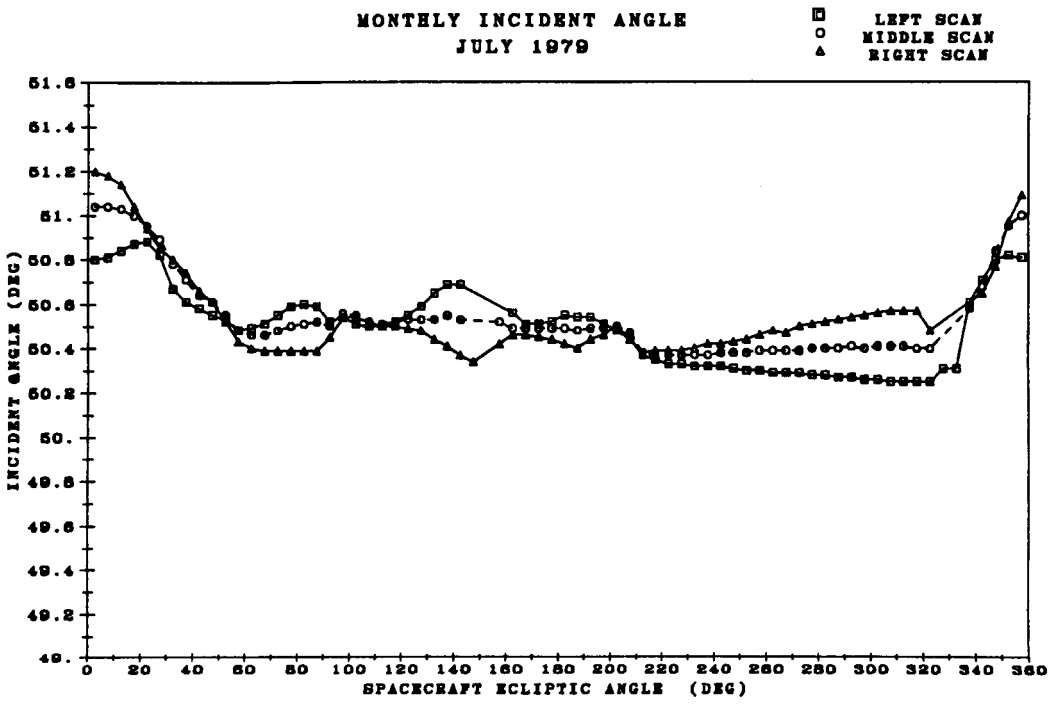

(b)

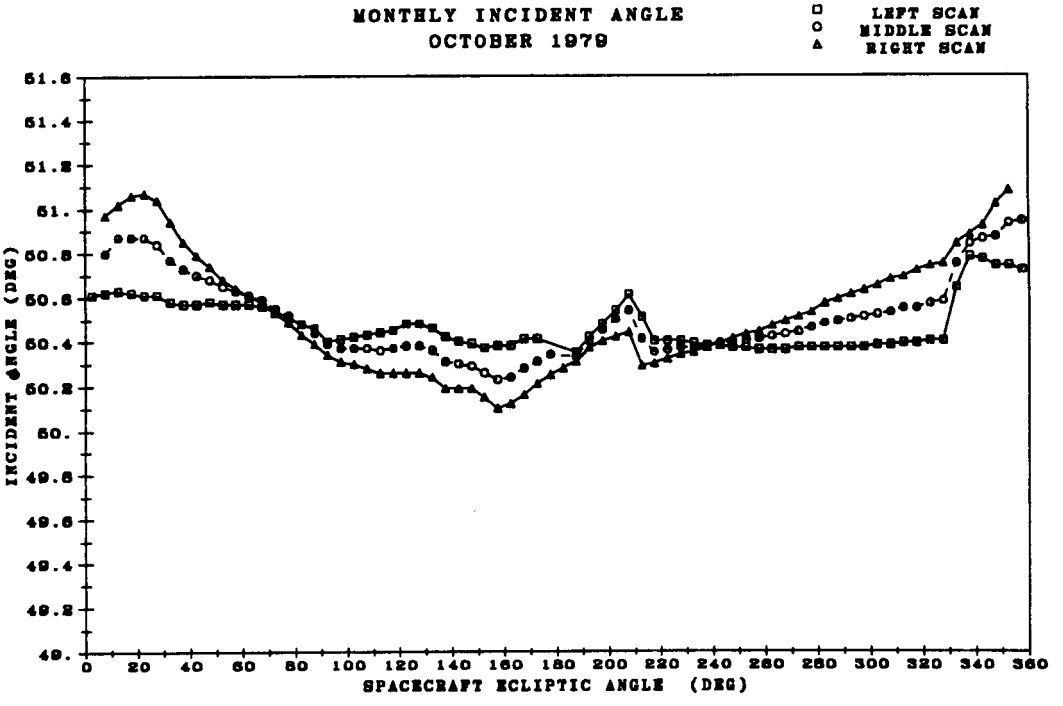

Figure 2.8 Monthly average incident angle in July 1979 (a) and October 1979 (b) for three scan positions as a function of spacecraft ecliptic angle.

(a)

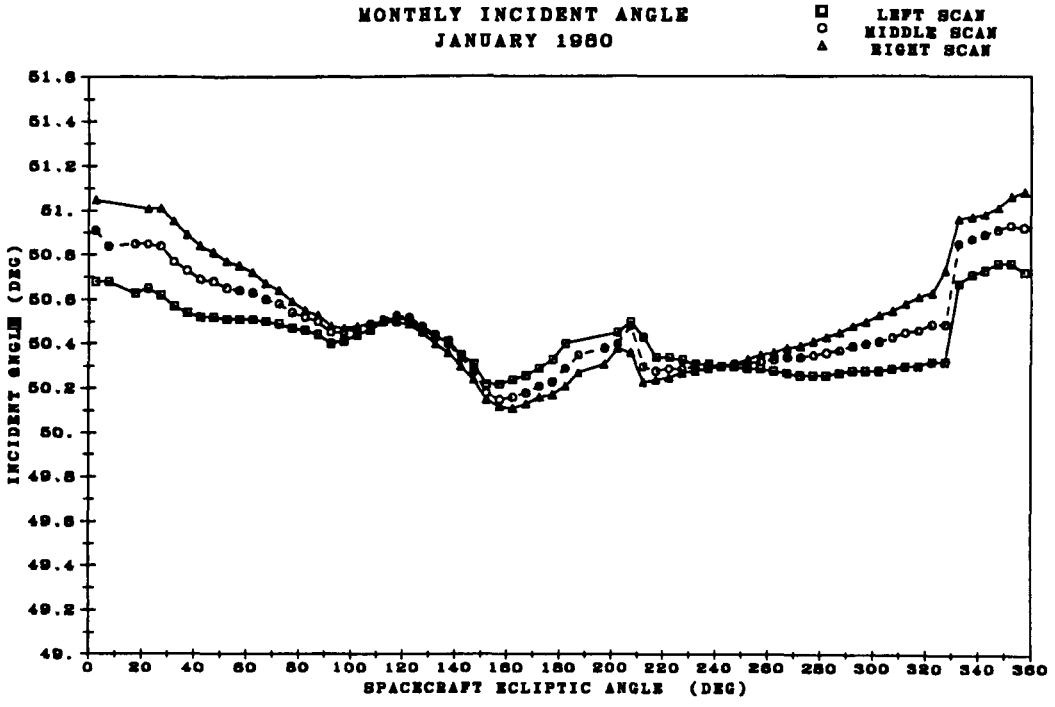

(b)

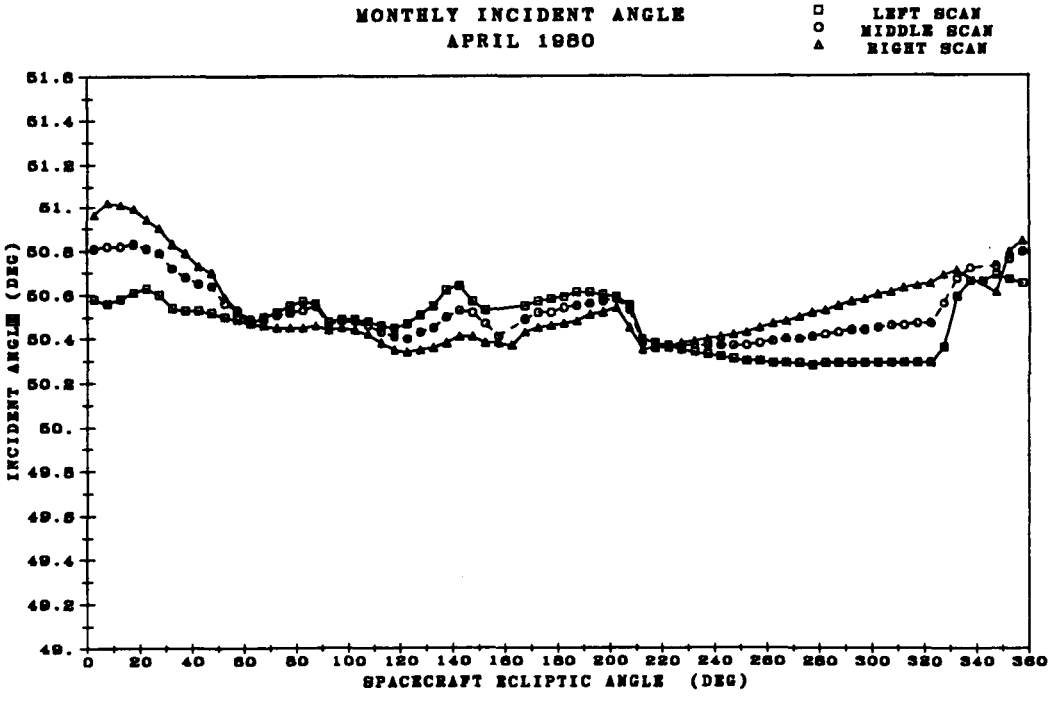

Figure 2.9 Monthly average incident angle in January 1980 (a) and April 1980 (b) for three scan positions as a function of spacecraft ecliptic angle.

(a)

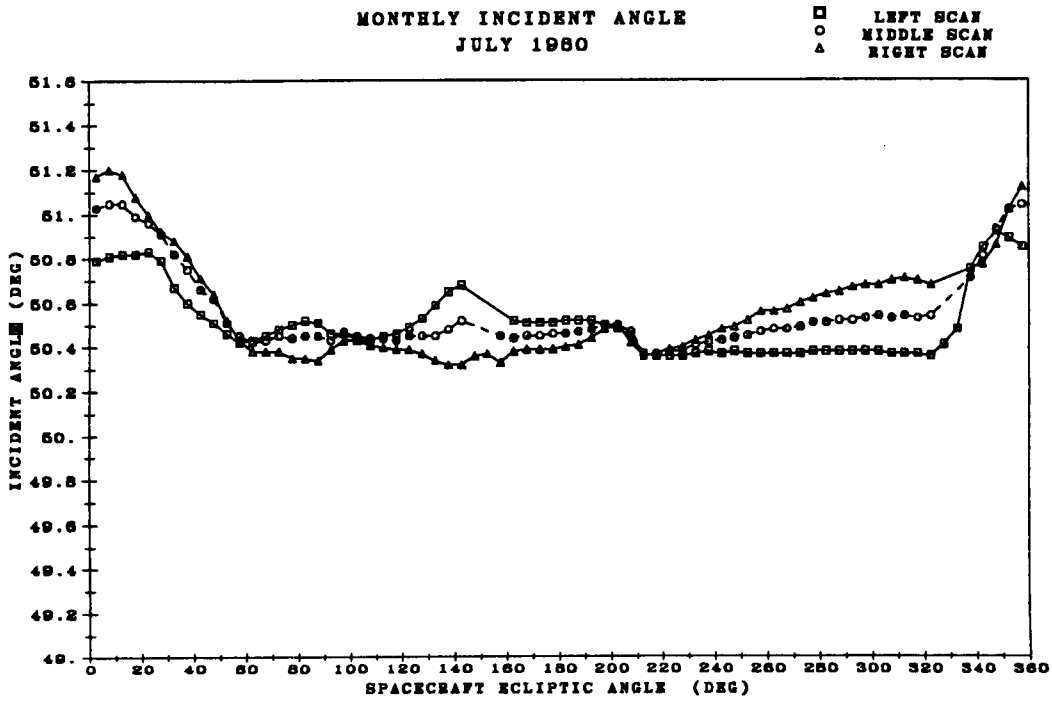

(b)

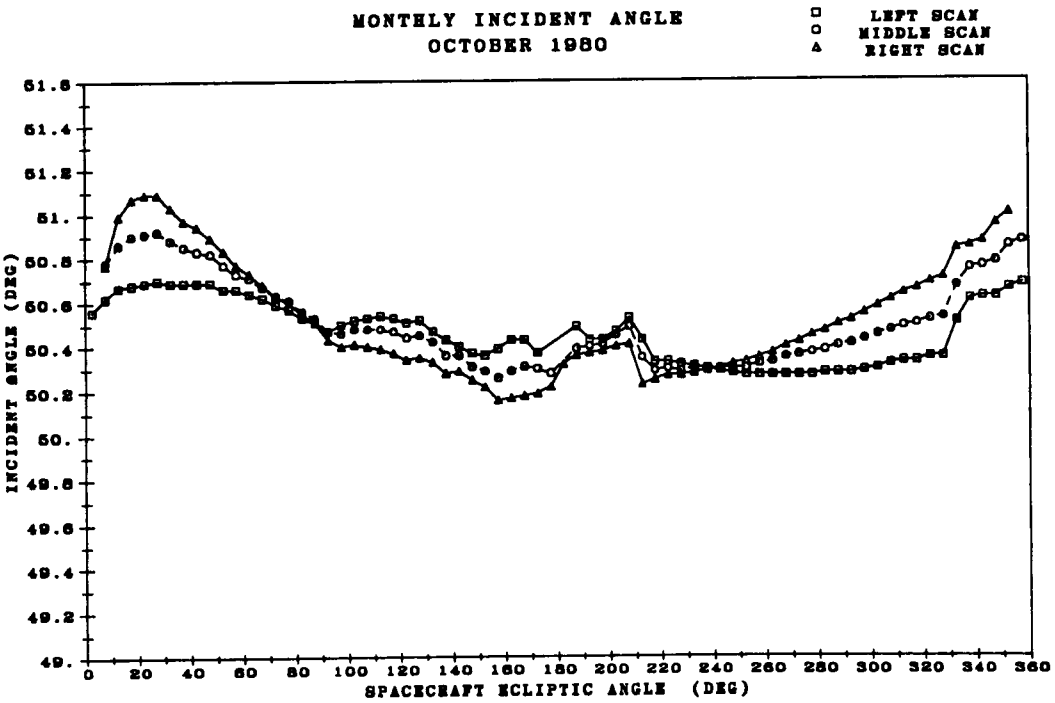

Figure 2.10 Monthly average incident angle in July 1980 (a) and October 1980 (b) for three scan positions as a function of spacecraft ecliptic angle.

(a)

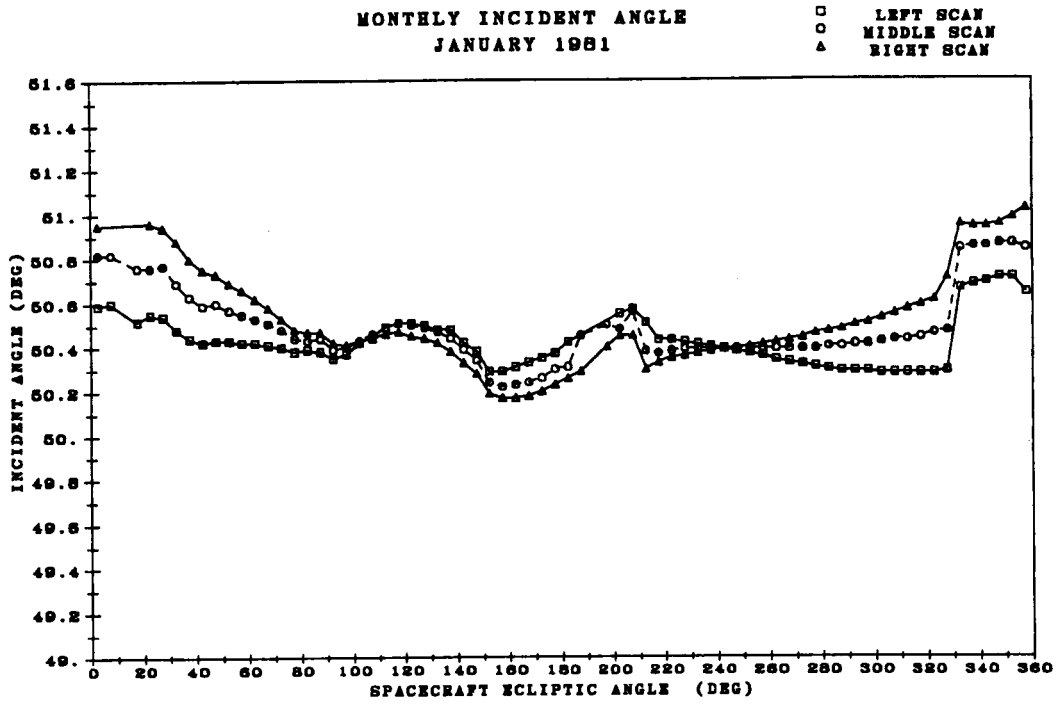

(b)

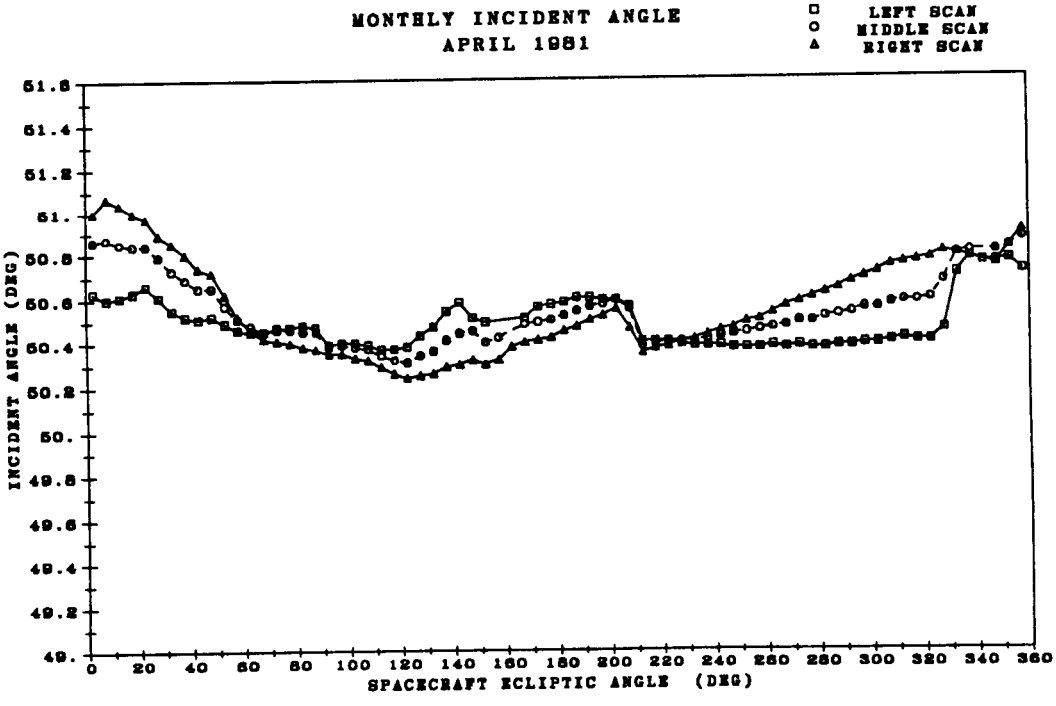

Figure 2.11 Monthly average incident angle in January 1981 (a) and April 1981 (b) for three scan positions as a function of spacecraft ecliptic angle.

(a)

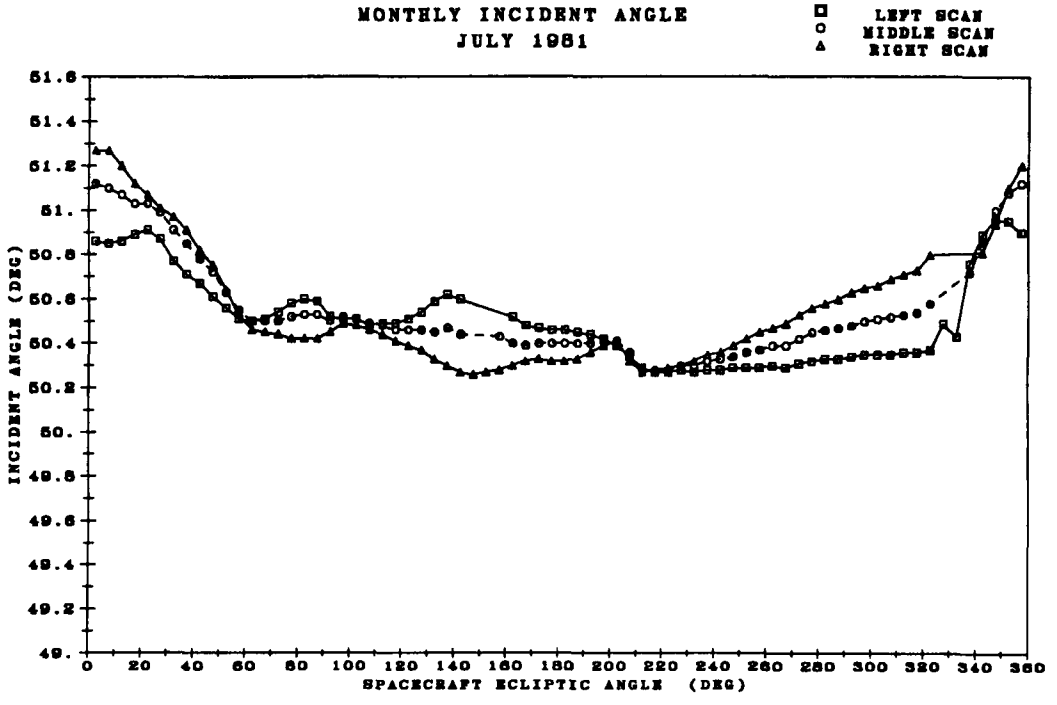

(b)

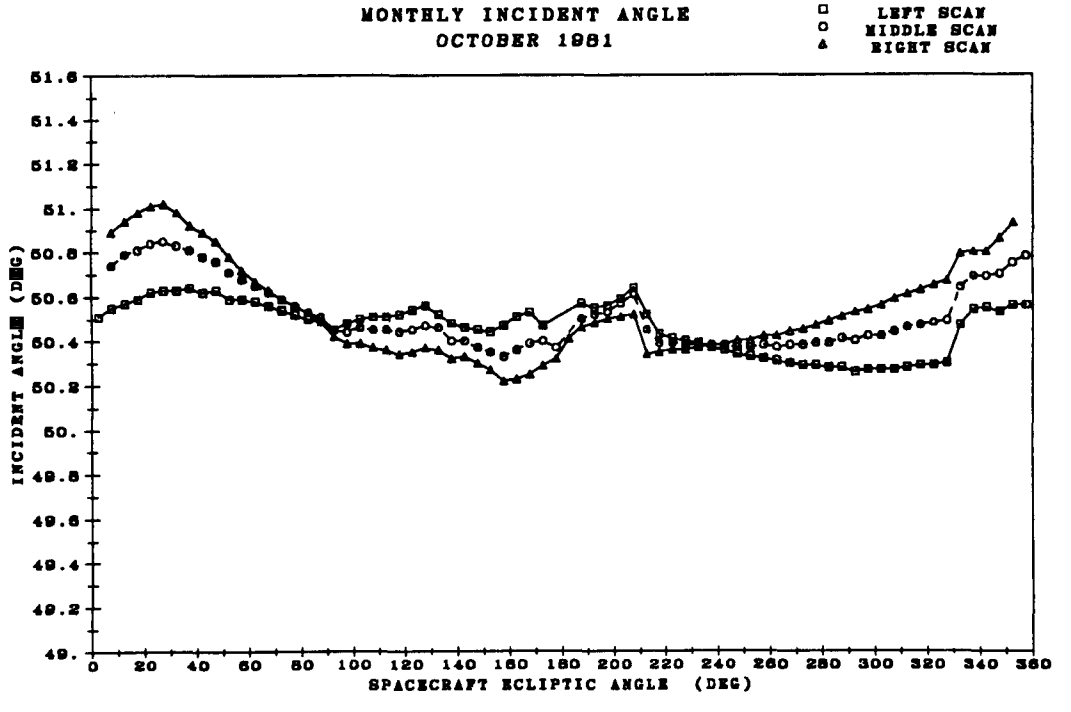

Figure 2.12 Monthly average incident angle in July 1981 (a) and October 1981 (b) for three scan positions as a function of spacecraft ecliptic angle.

(a)

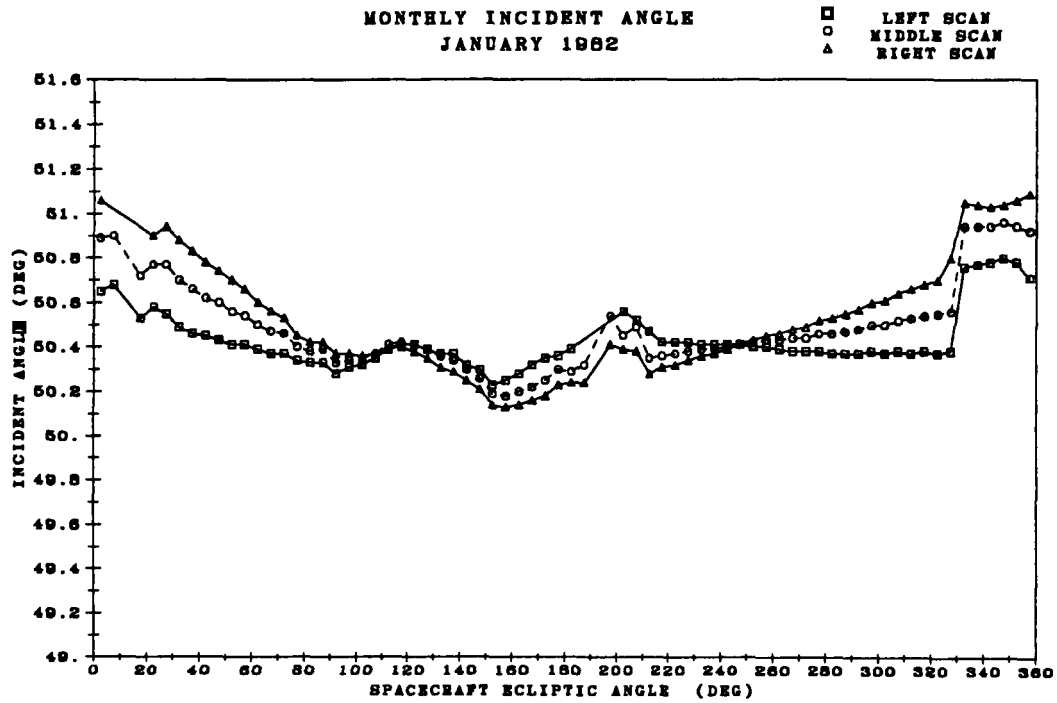

(b)

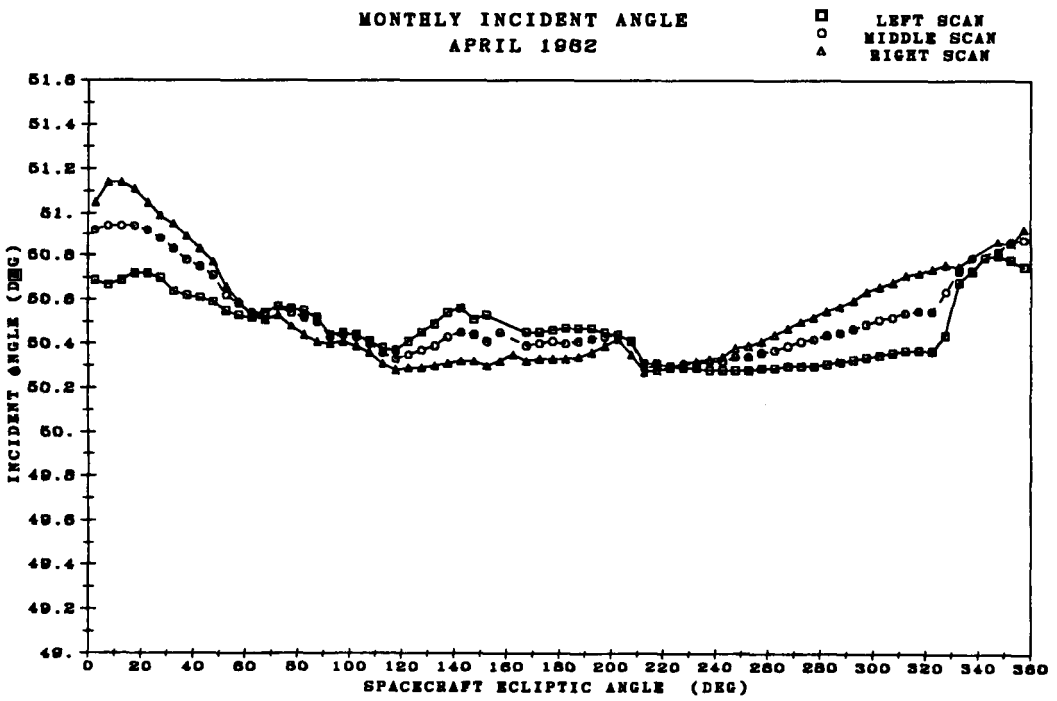

Figure 2.13 Monthly average incident angle in January 1982 (a) and April 1982 (b) for three scan positions as a function of spacecraft ecliptic angle.

(a)

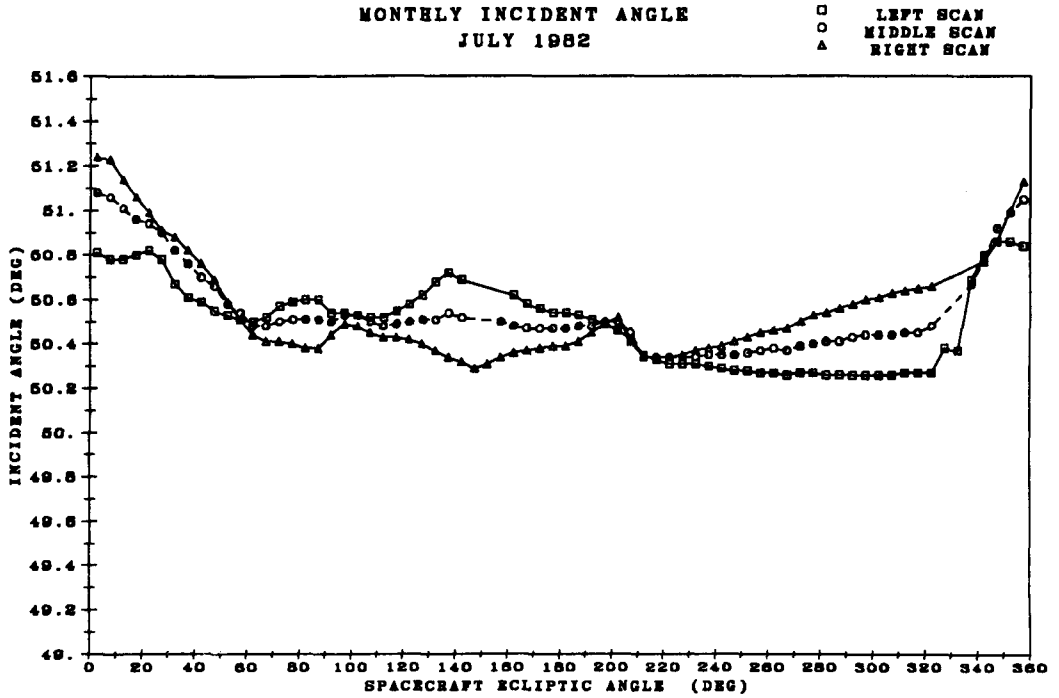

(b)

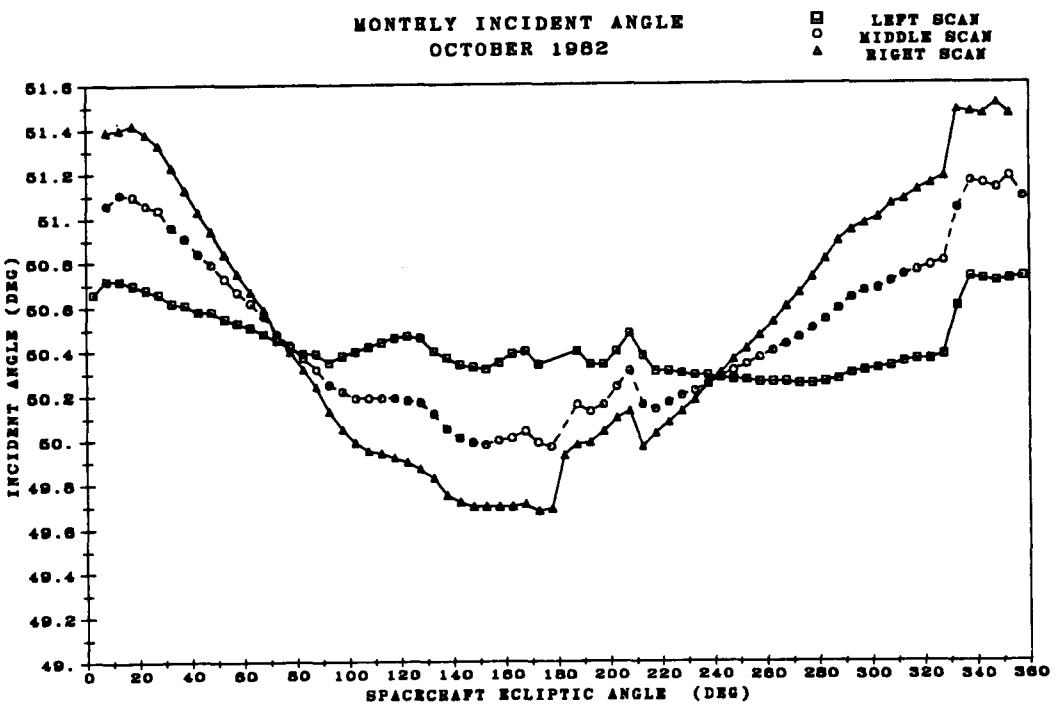

Figure 2.14 Monthly average incident angle in July 1982 (a) and October 1982 (b) for three scan positions as a function of spacecraft ecliptic angle.

(a)

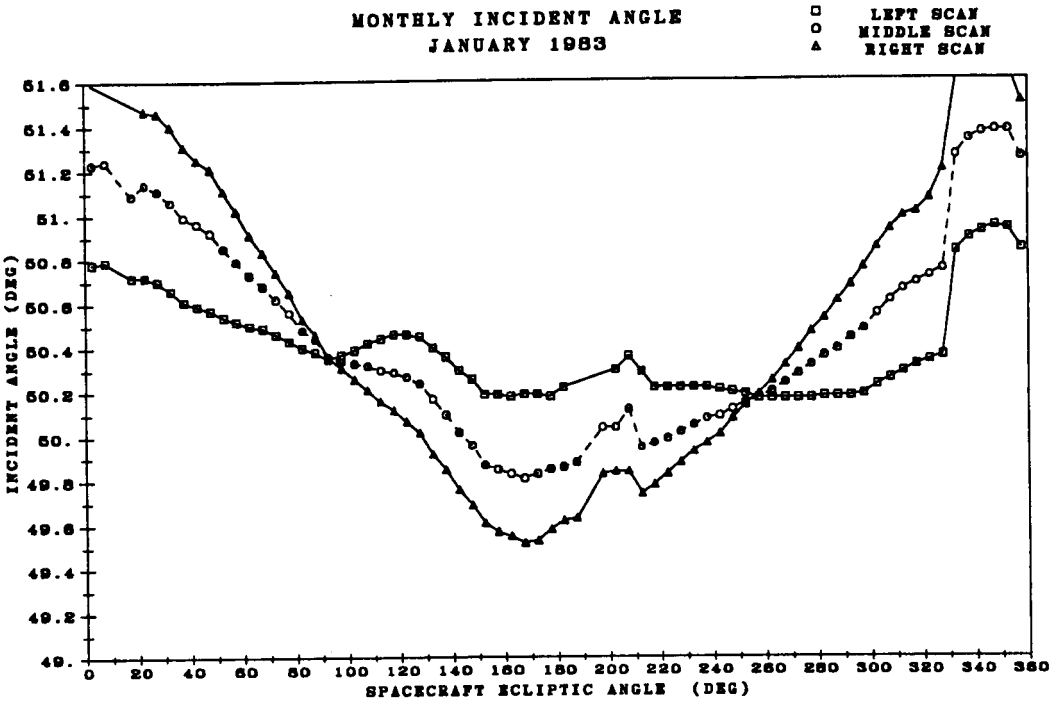

(b)

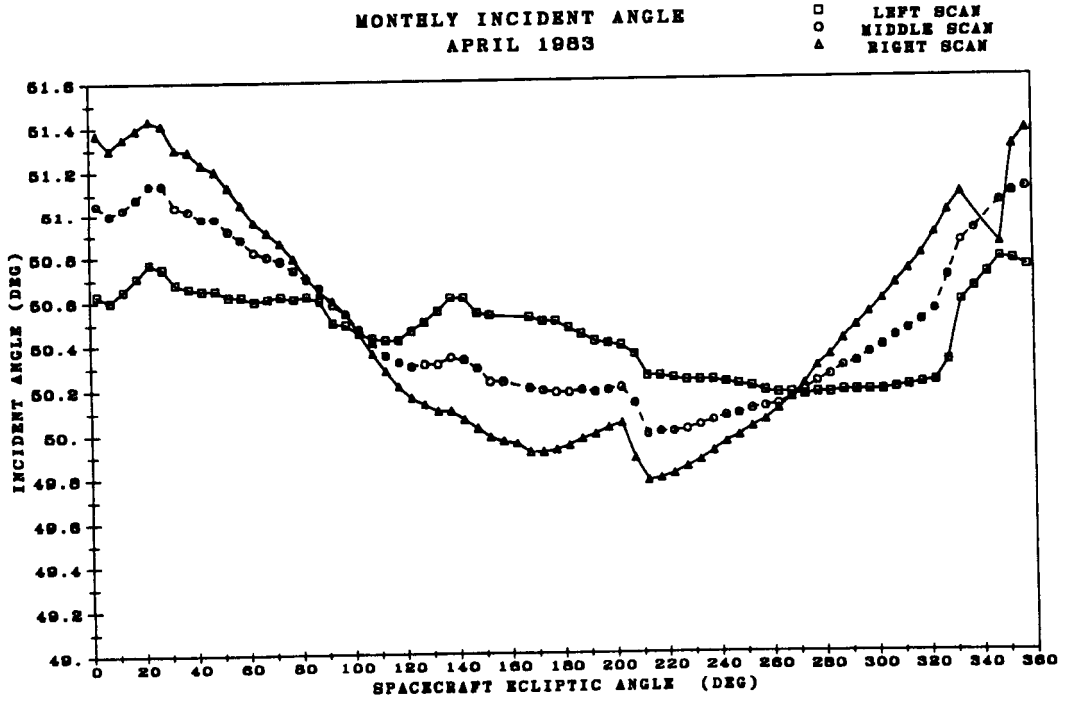

Figure 2.15 Monthly average incident angle in January 1983 (a) and April 1983 (b) for three scan positions as a function of spacecraft ecliptic angle.

(a)

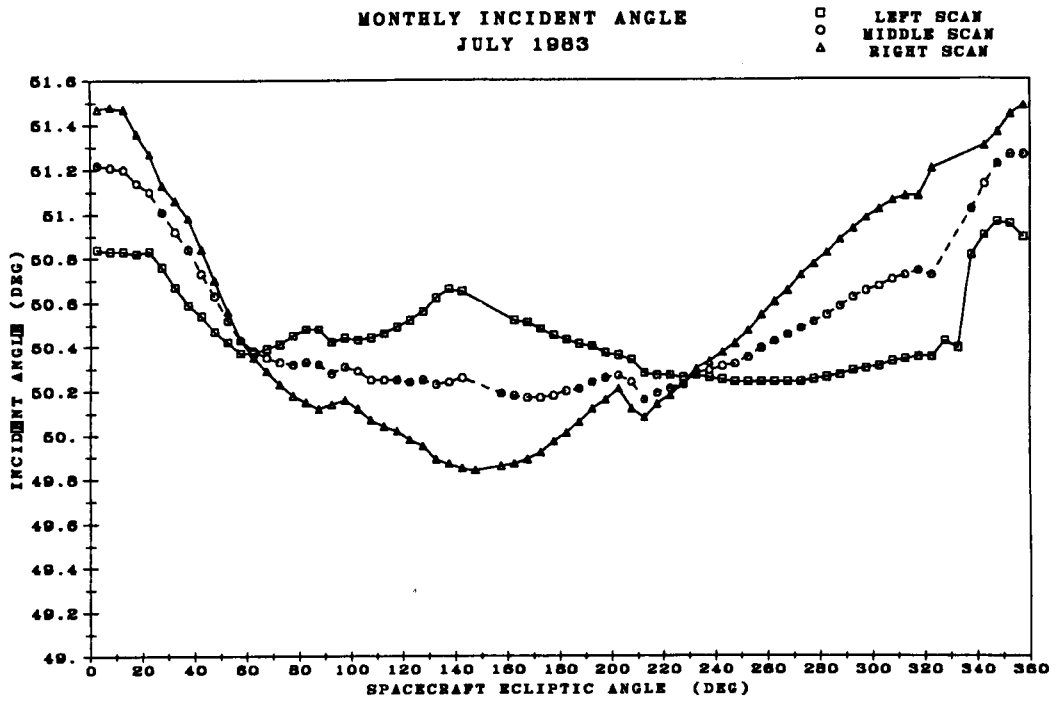

(b)

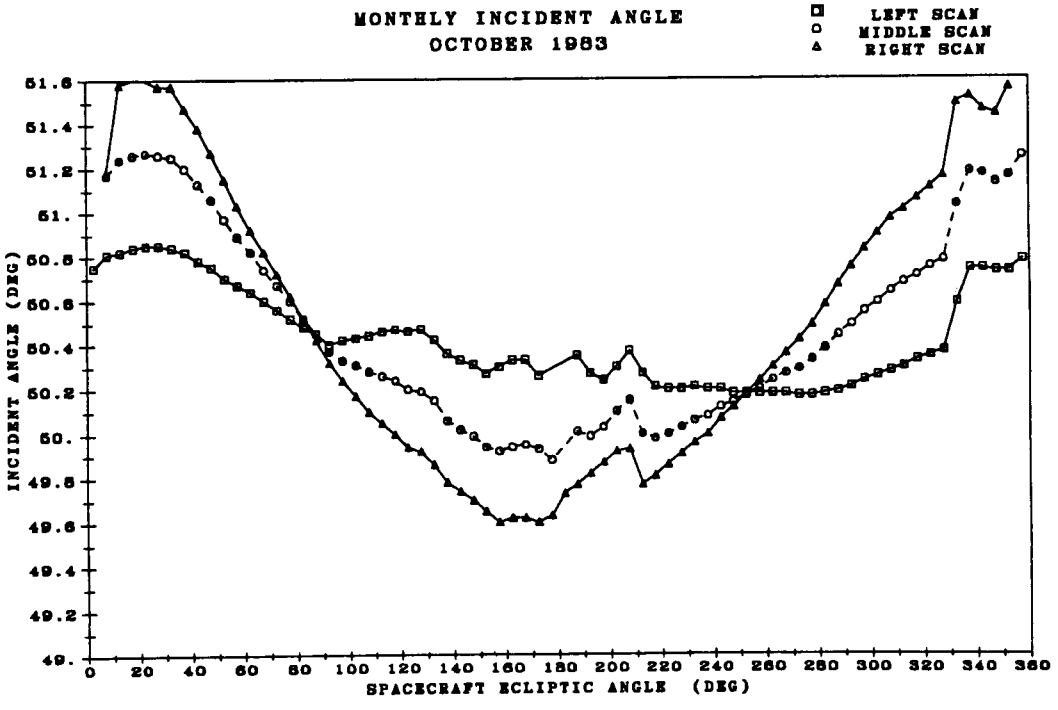

Figure 2.16 Monthly average incident angle in July 1983 (a) and October 1983 (b) for three scan positions as a function of spacecraft ecliptic angle.

(a)

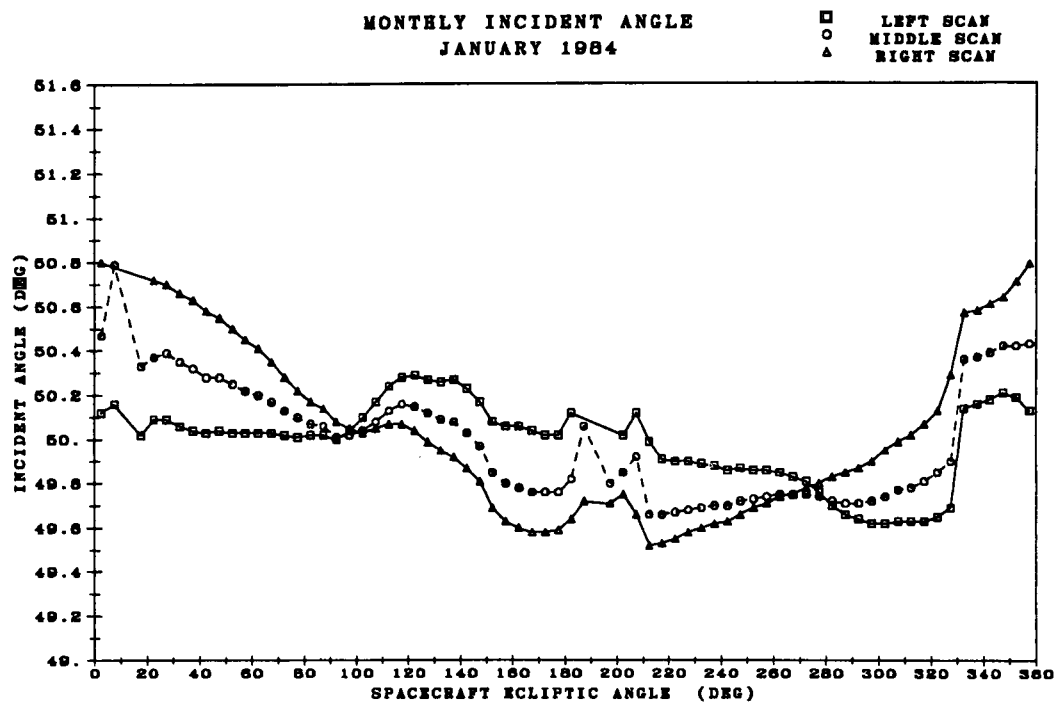

(b)

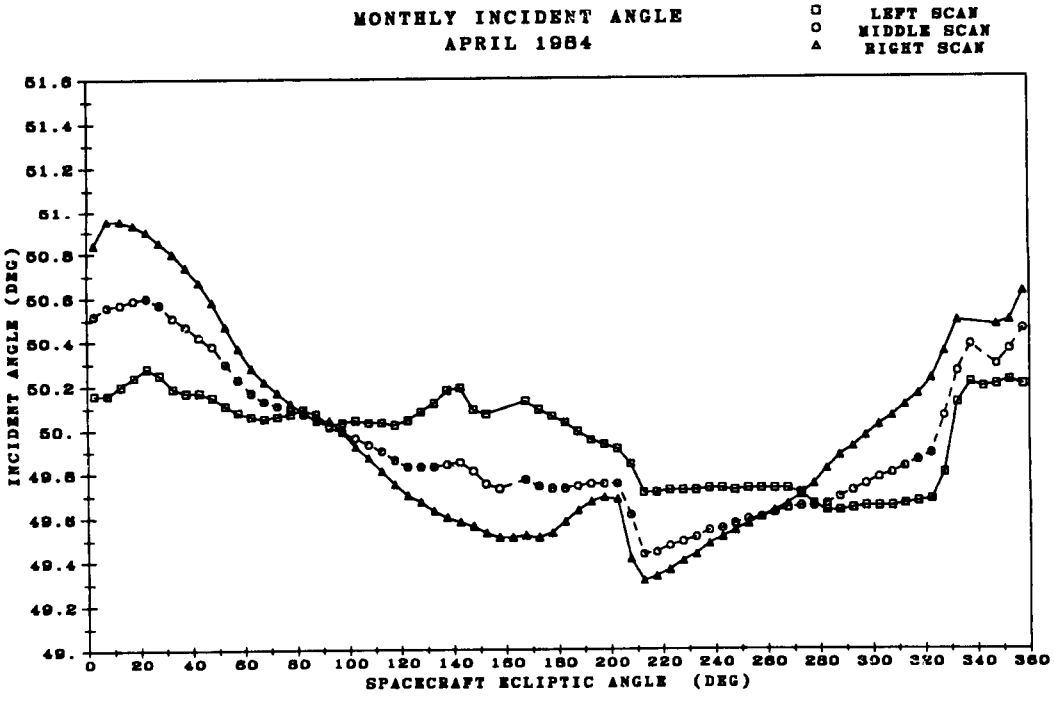

Figure 2.17 Monthly average incident angle in January 1984 (a) and April 1984 (b) for three scan positions as a function of spacecraft ecliptic angle.

(a)

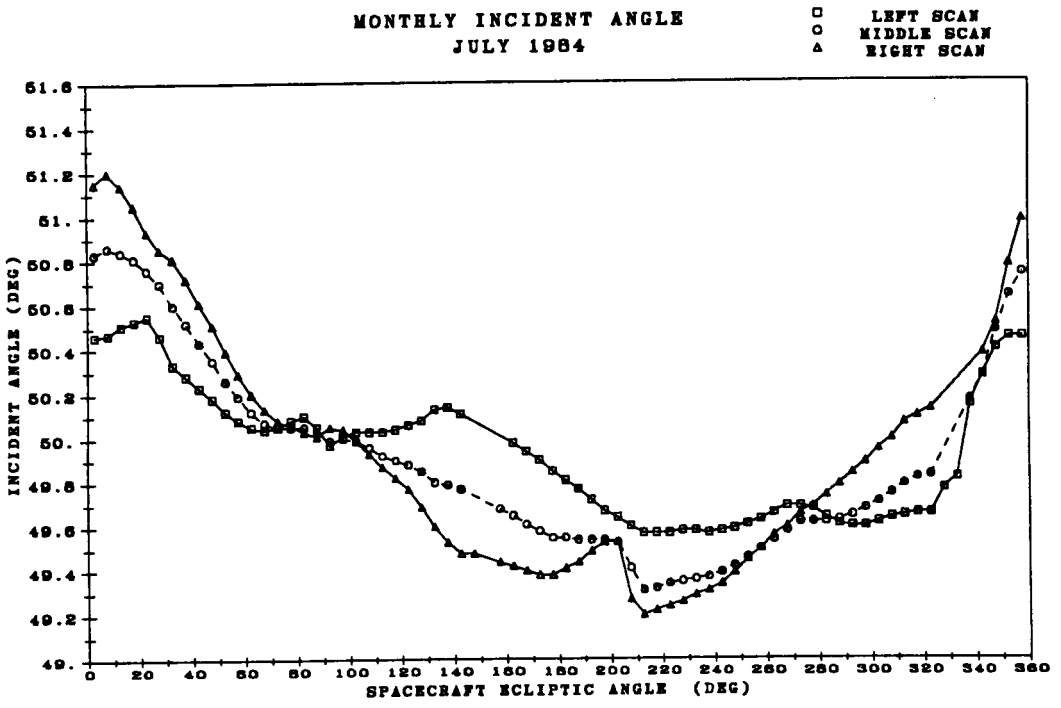

(b)

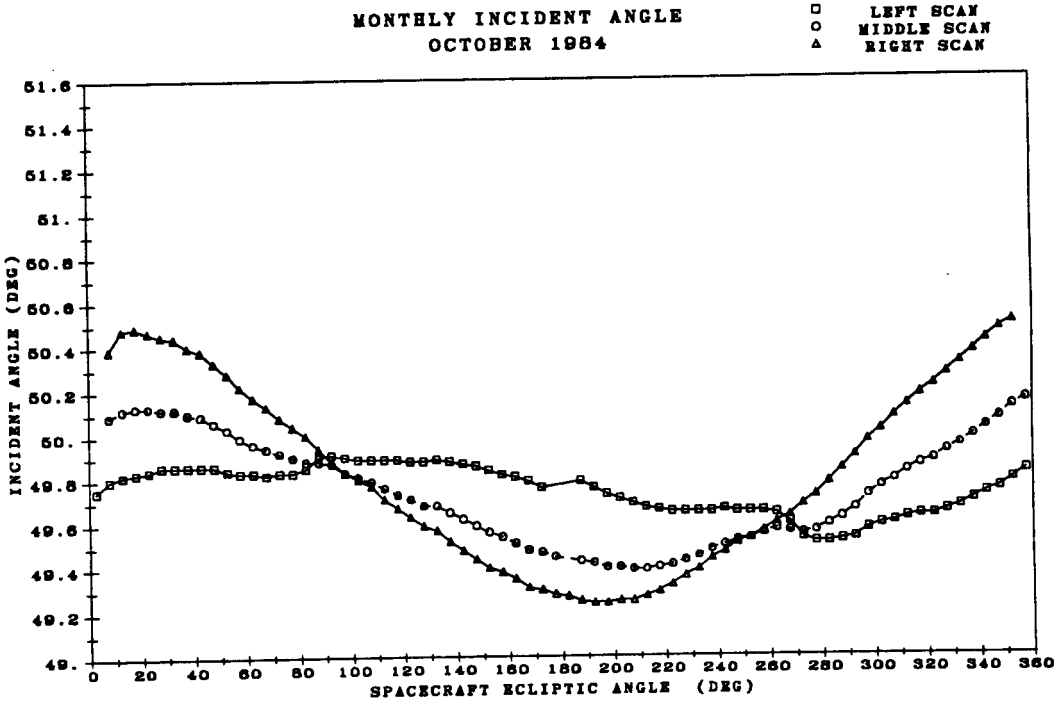

Figure 2.18 Monthly average incident angle in July 1984 (a) and October 1984 (b) for three scan positions as a function of spacecraft ecliptic angle.

(a)

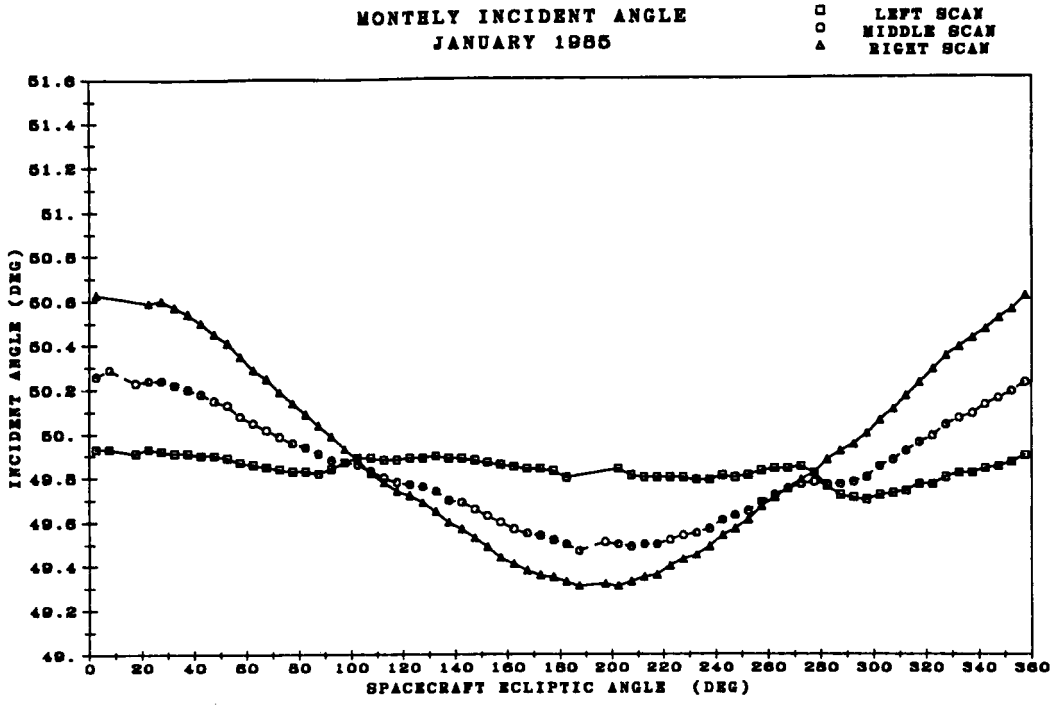

(b)

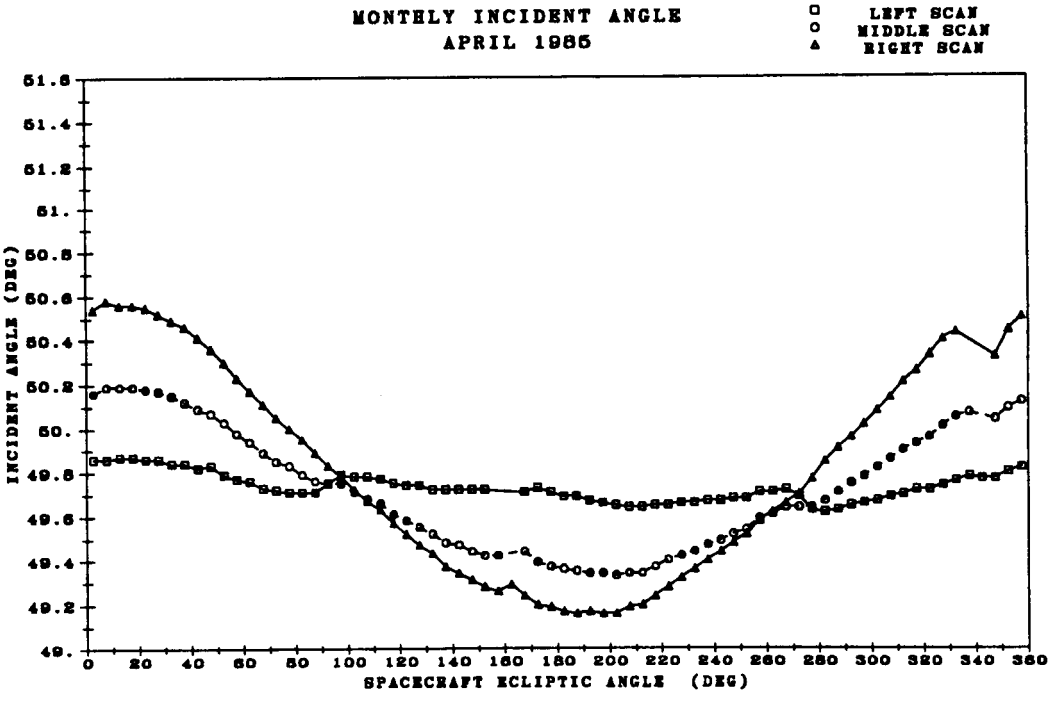

Figure 2.19 Monthly average incident angle in January 1985 (a) and April 1985 (b) for three scan positions as a function of spacecraft ecliptic angle.

(a)

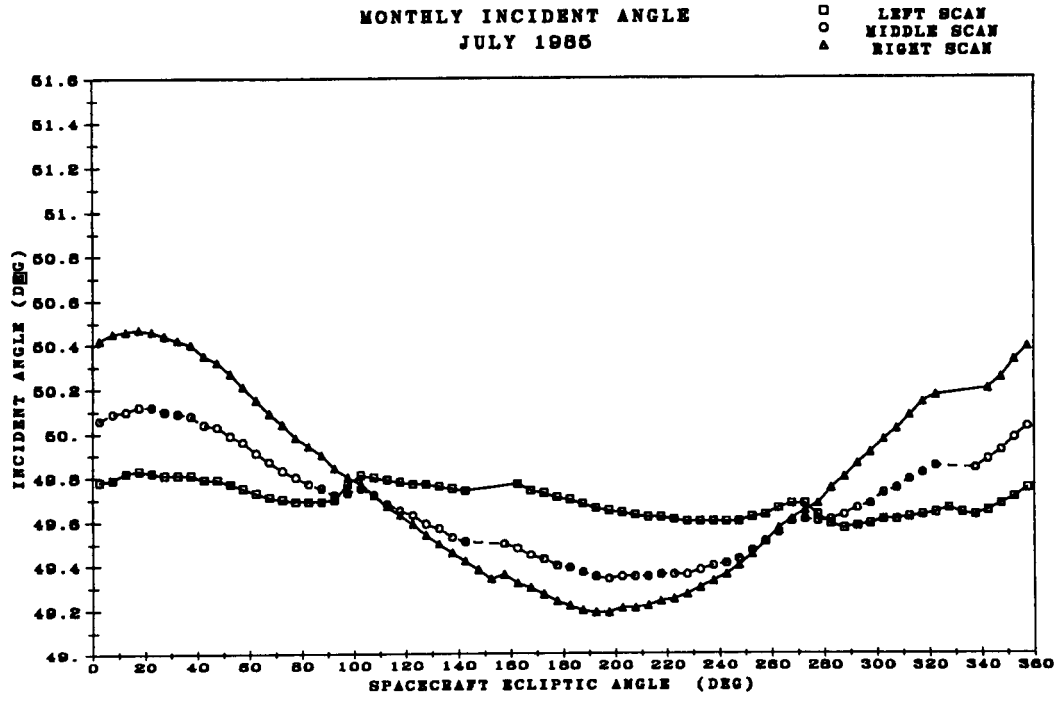

(b)

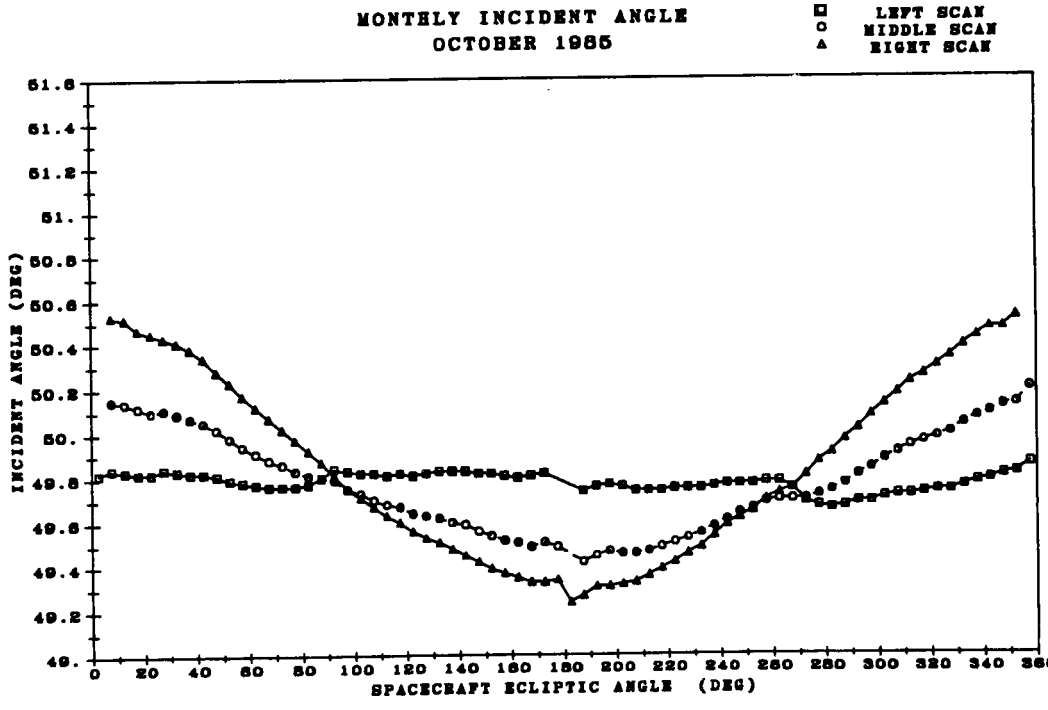

Figure 2.20 Monthly average incident angle in July 1985 (a) and October 1985 (b) for three scan positions as a function of spacecraft ecliptic angle.

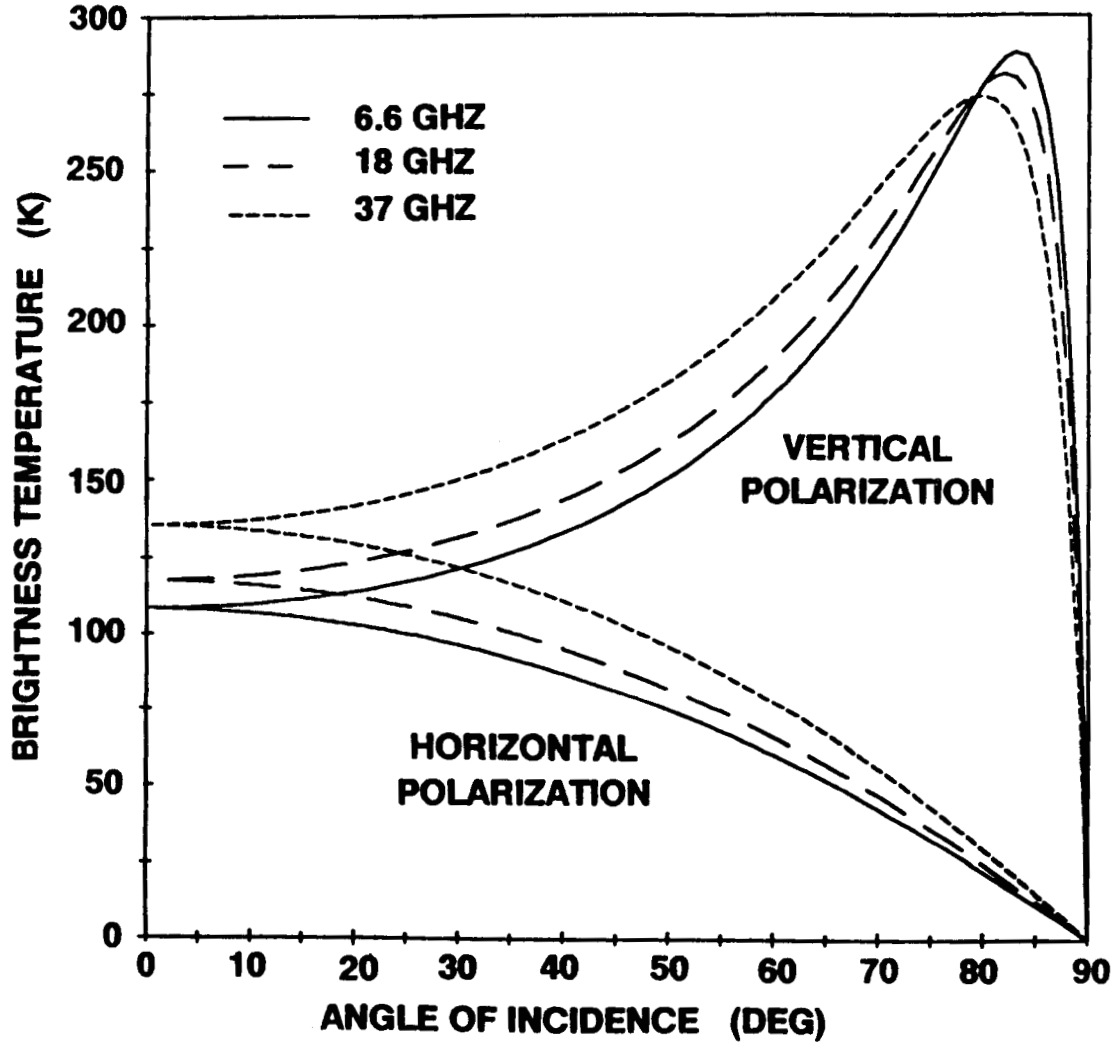

Figure 3.1 Brightness temperature at three of the SMMR frequencies for a smooth ocean surface and no atmosphere.

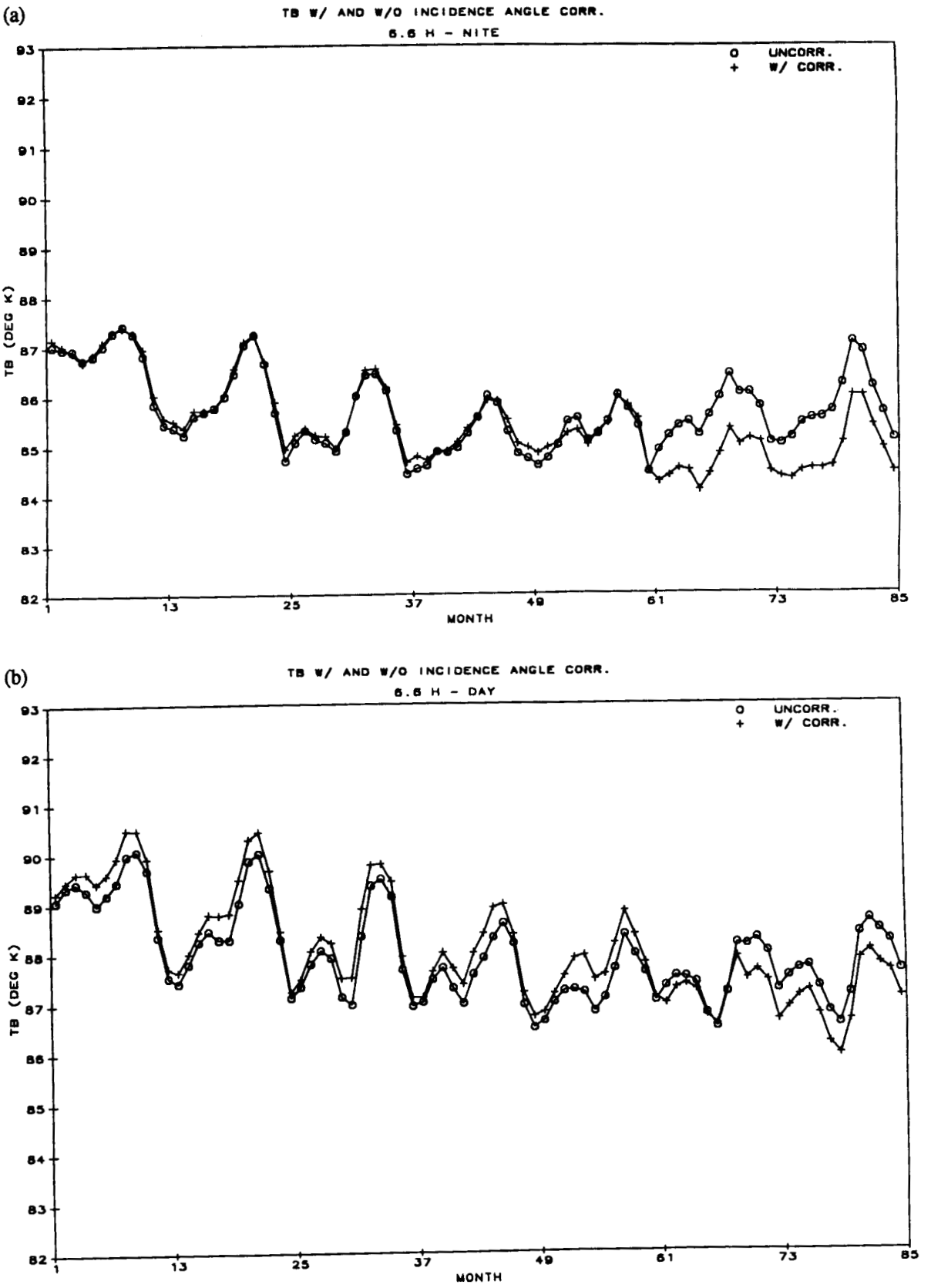

Figure 3.2 Monthly average nighttime (a) and daytime (b) SMMR 6.6 GHz horizontal brightness temperature over ocean areas between 60 deg N and 60 deg S before and after incident angle correction.

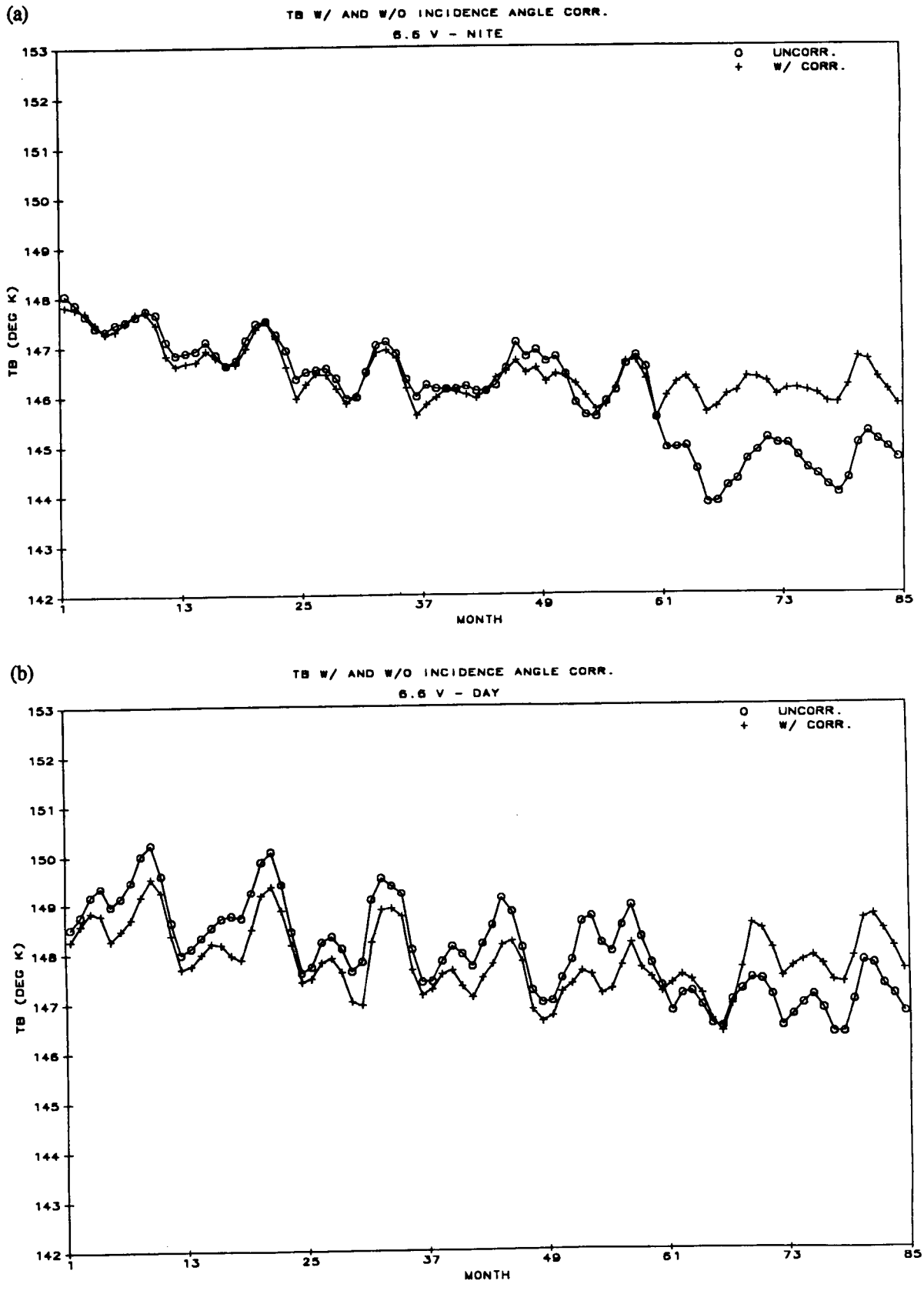

Figure 3.3 Monthly average nighttime (a) and daytime (b) SMMR 6.6 GHz vertical brightness temperature over ocean areas between 60 deg N and 60 deg S before and after incident angle correction.

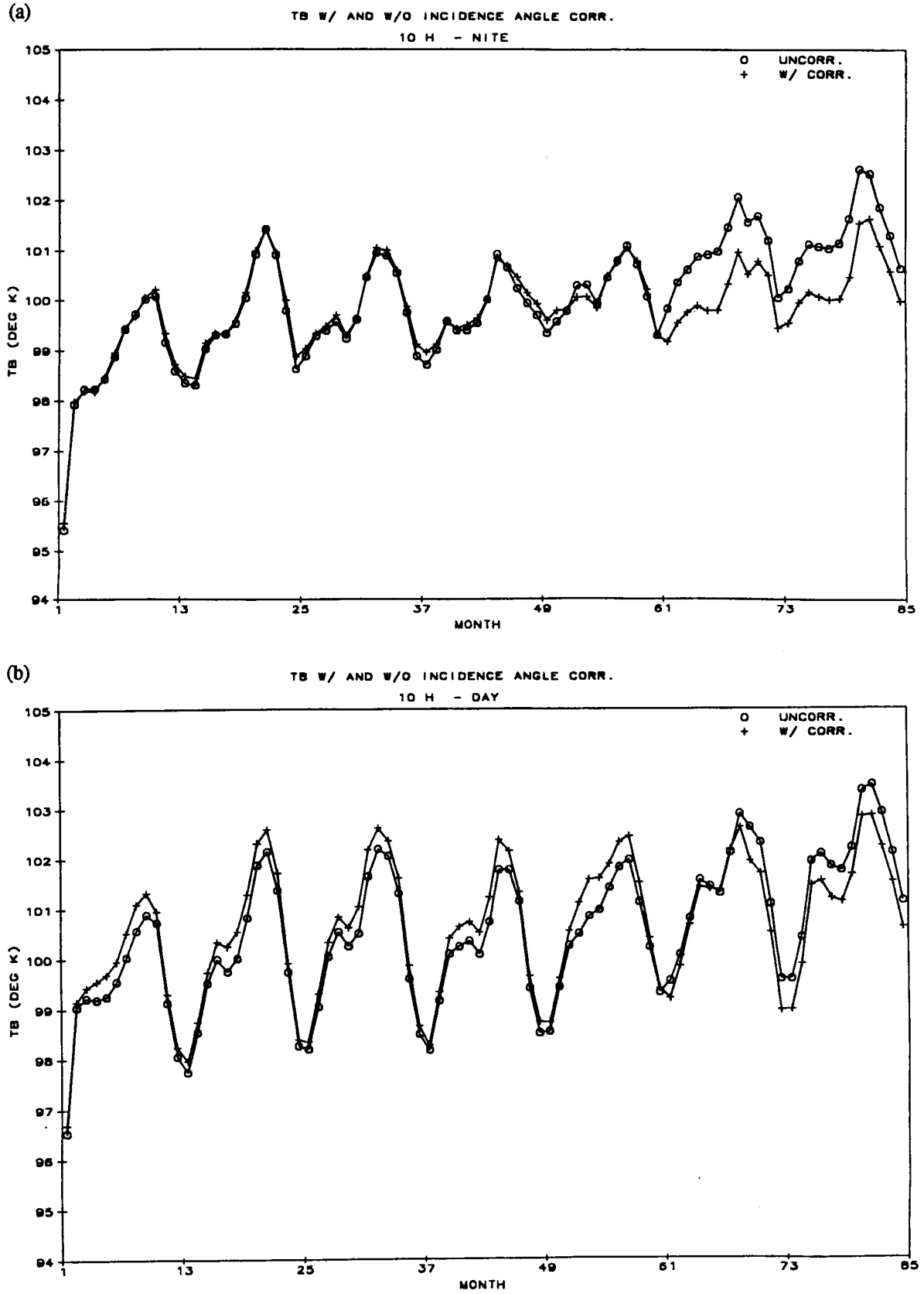

Figure 3.4 Monthly average nighttime (a) and daytime (b) SMMR 10.7 GHz horizontal brightness temperature over ocean areas between 60 deg N and 60 deg S before and after incident angle correction.

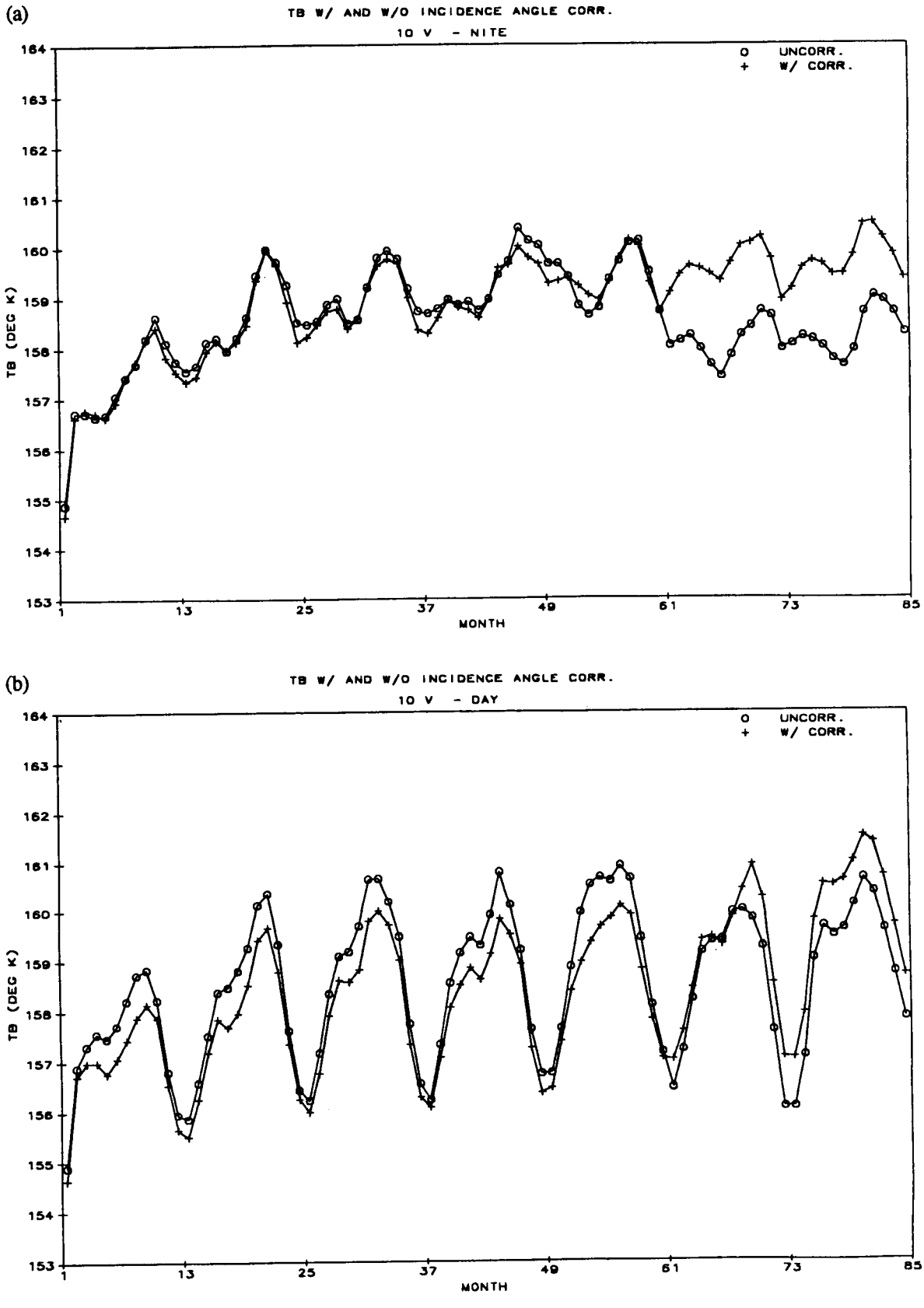

Figure 3.5 Monthly average nighttime (a) and daytime (b) SMMR 10.7 GHz vertical brightness temperature over ocean areas between 60 deg N and 60 deg S before and after incident angle correction.

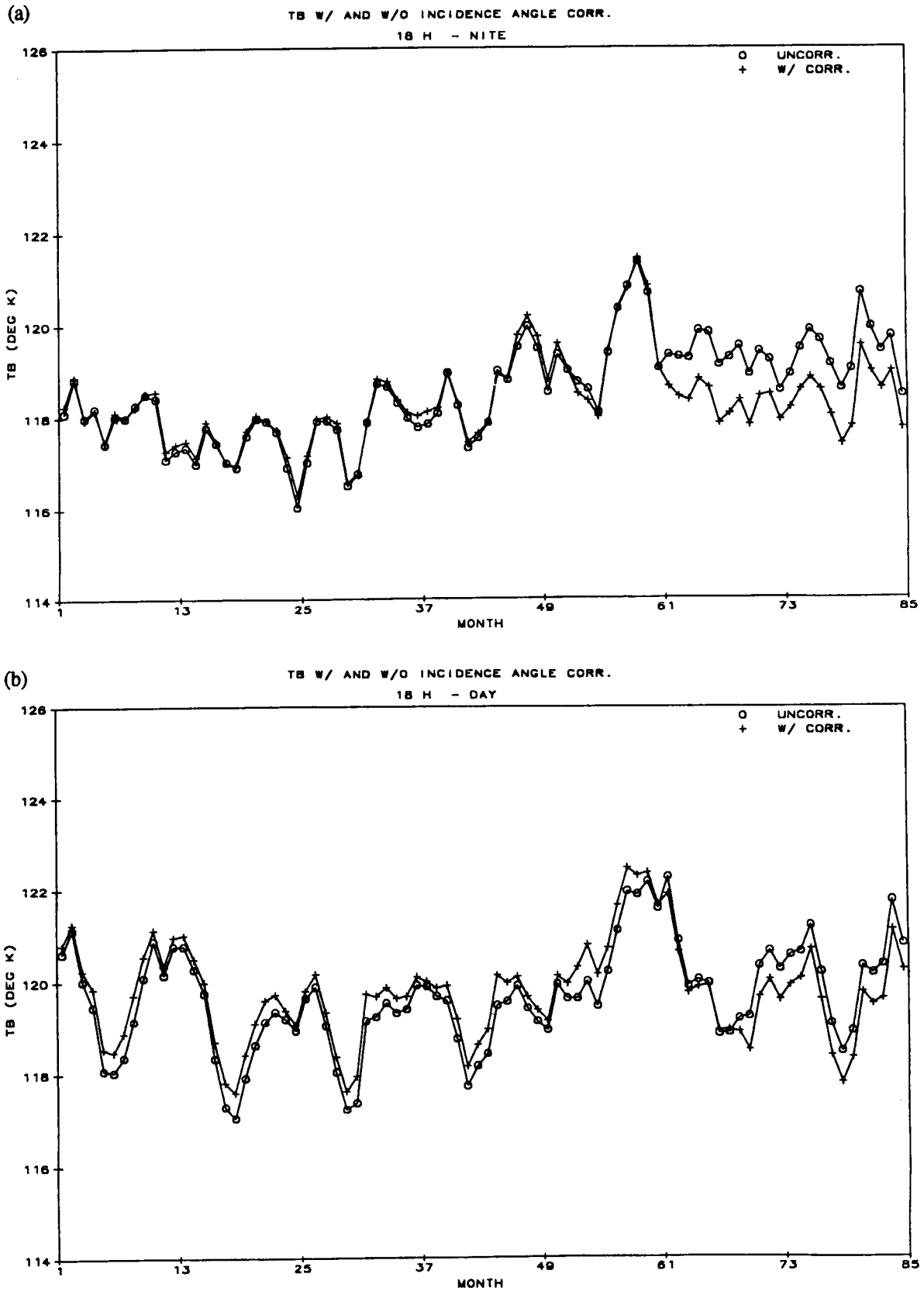

Figure 3.6 Monthly average nighttime (a) and daytime (b) SMMR 18.0 GHz horizontal brightness temperature over ocean areas between 60 deg N and 60 deg S before and after incident angle correction.

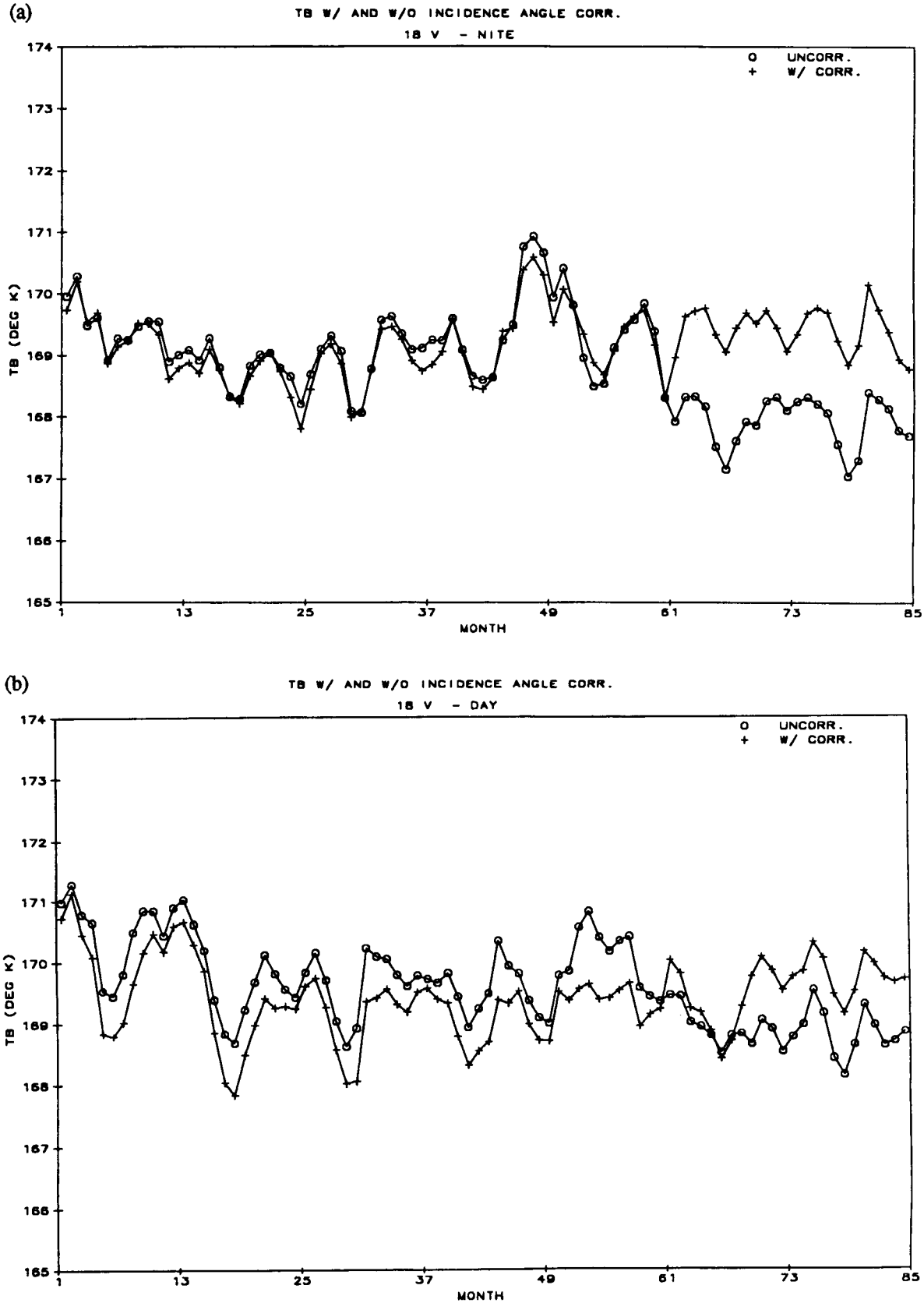

Figure 3.7 Monthly average nighttime (a) and daytime (b) SMMR 18.0 GHz vertical brightness temperature over ocean areas between 60 deg N and 60 deg S before and after incident angle correction.

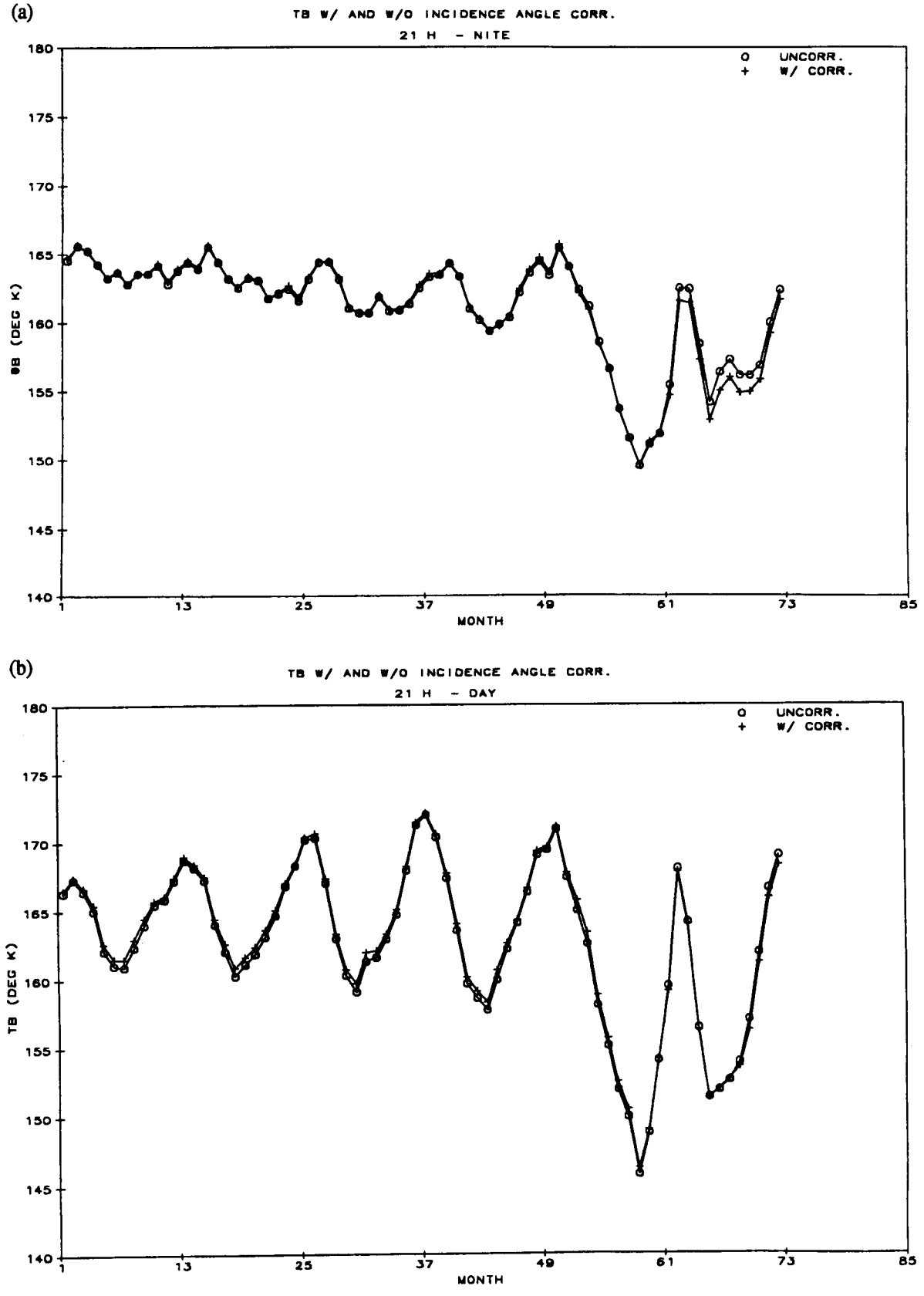

Figure 3.8 Monthly average nighttime (a) and daytime (b) SMMR 21.0 GHz horizontal brightness temperature over ocean areas between 60 deg N and 60 deg S before and after incident angle correction.

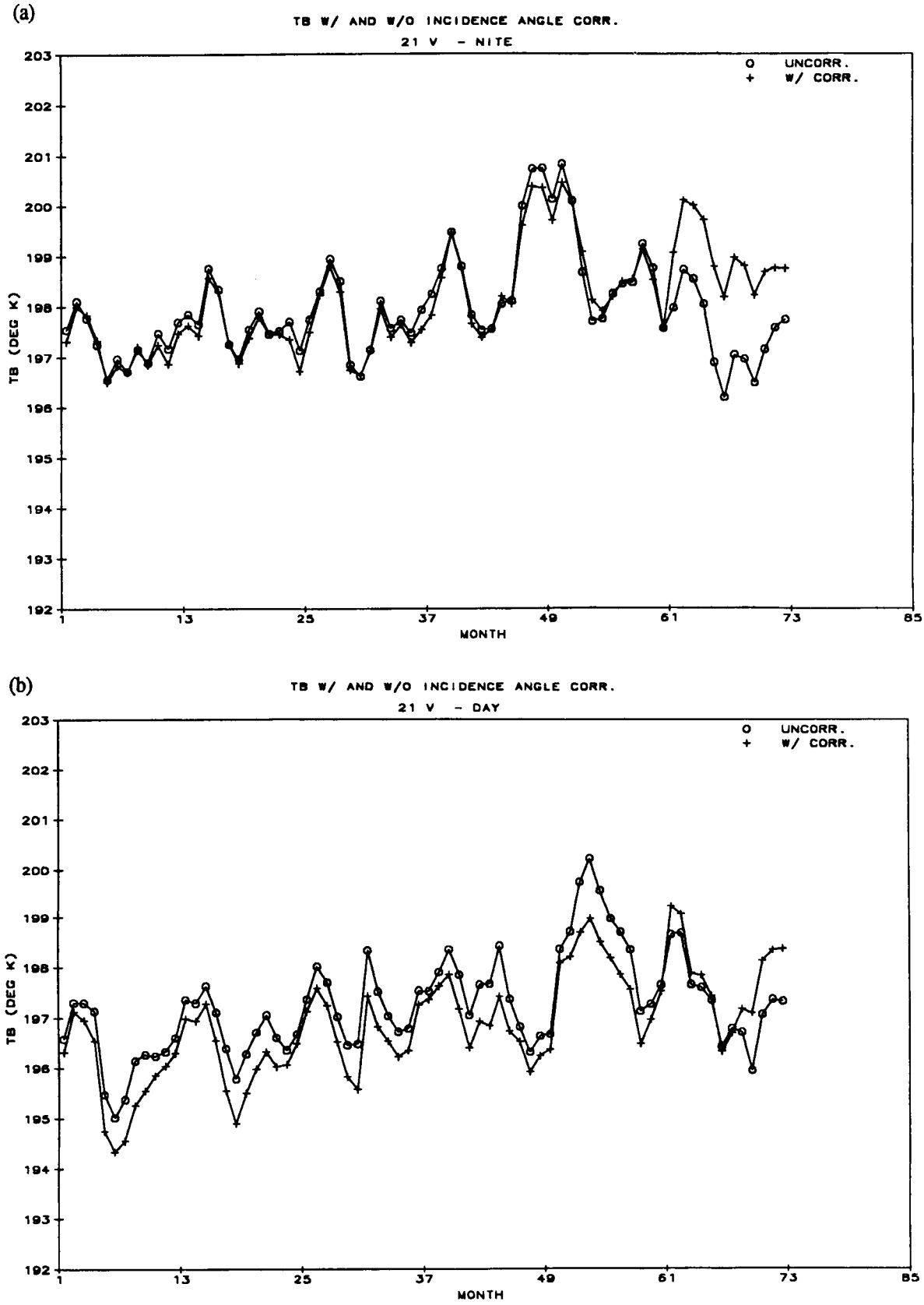

Figure 3.9 Monthly average nighttime (a) and daytime (b) SMMR 21.0 GHz vertical brightness temperature over ocean areas between 60 deg N and 60 deg S before and after incident angle correction.

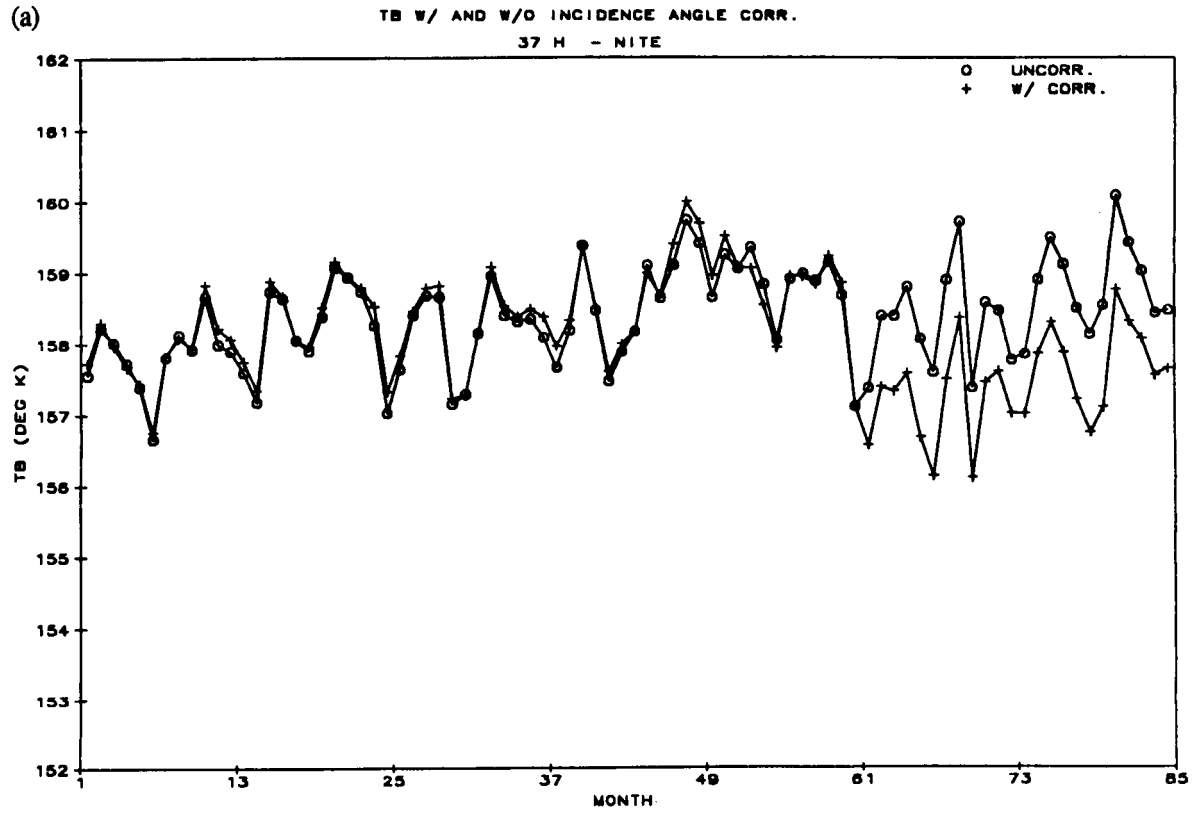

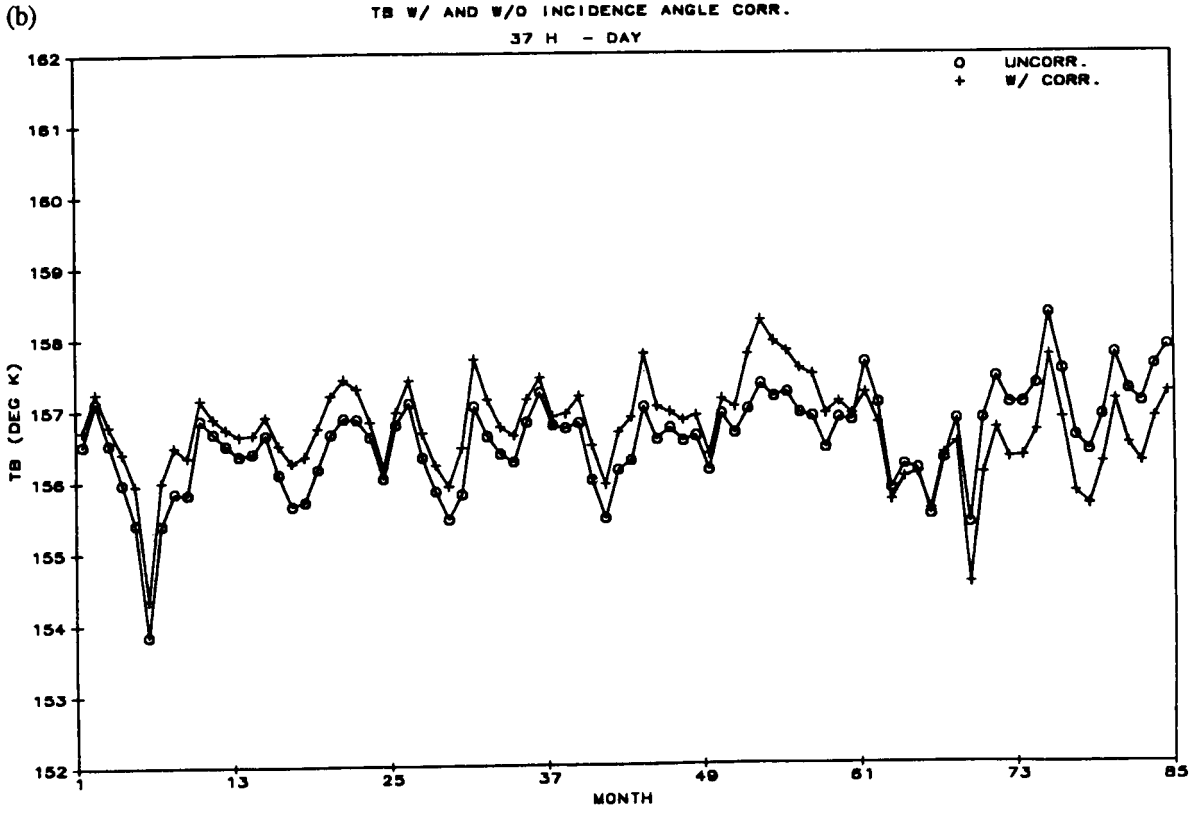

Figure 3.10 Monthly average nighttime (a) and daytime (b) SMMR 37.0 GHz horizontal brightness temperature over ocean areas between 60 deg N and 60 deg S before and after incident angle correction.

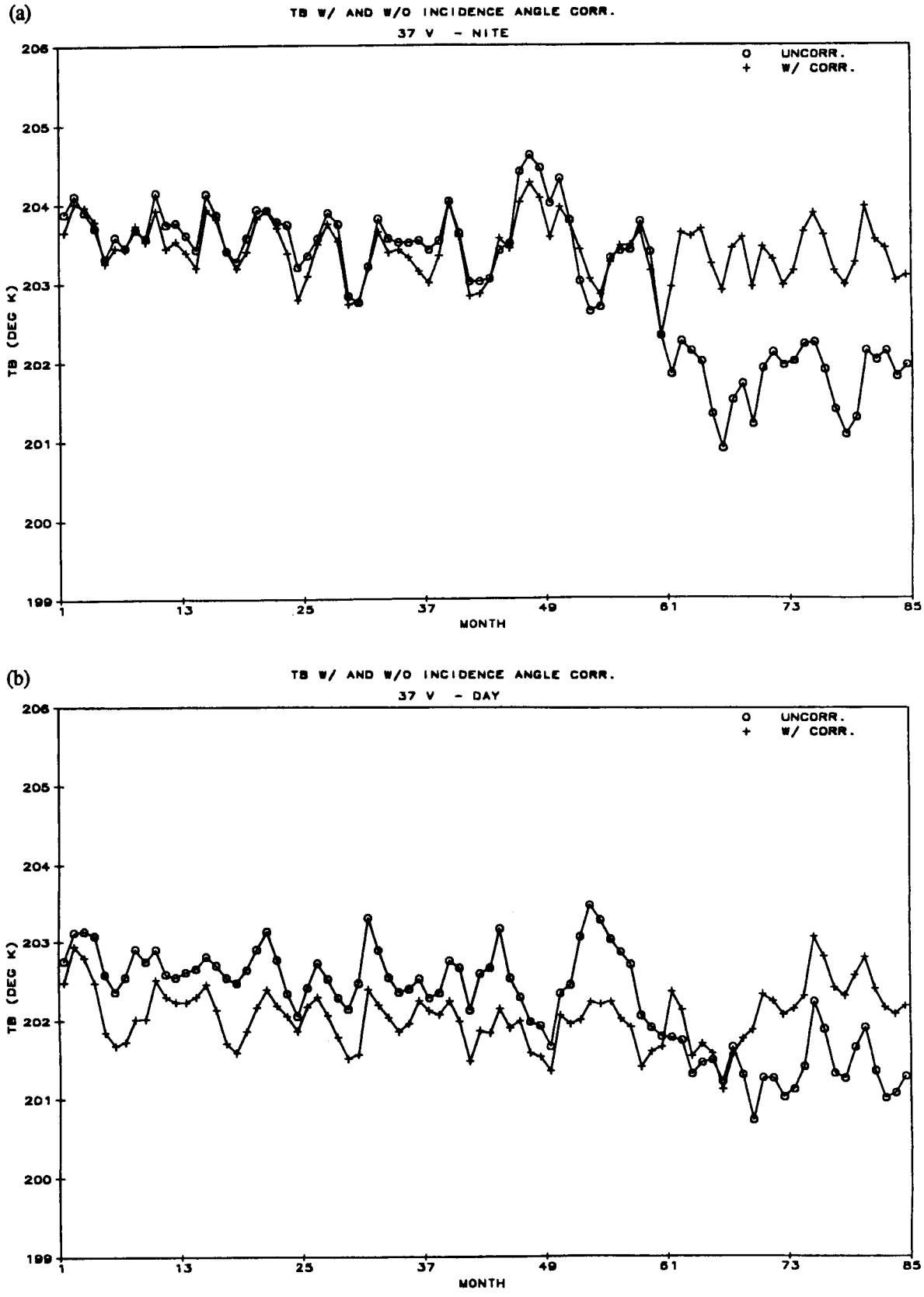

Figure 3.11 Monthly average nighttime (a) and daytime (b) SMMR 37.0 GHz vertical brightness temperature over ocean areas between 60 deg N and 60 deg S before and after incident angle correction.

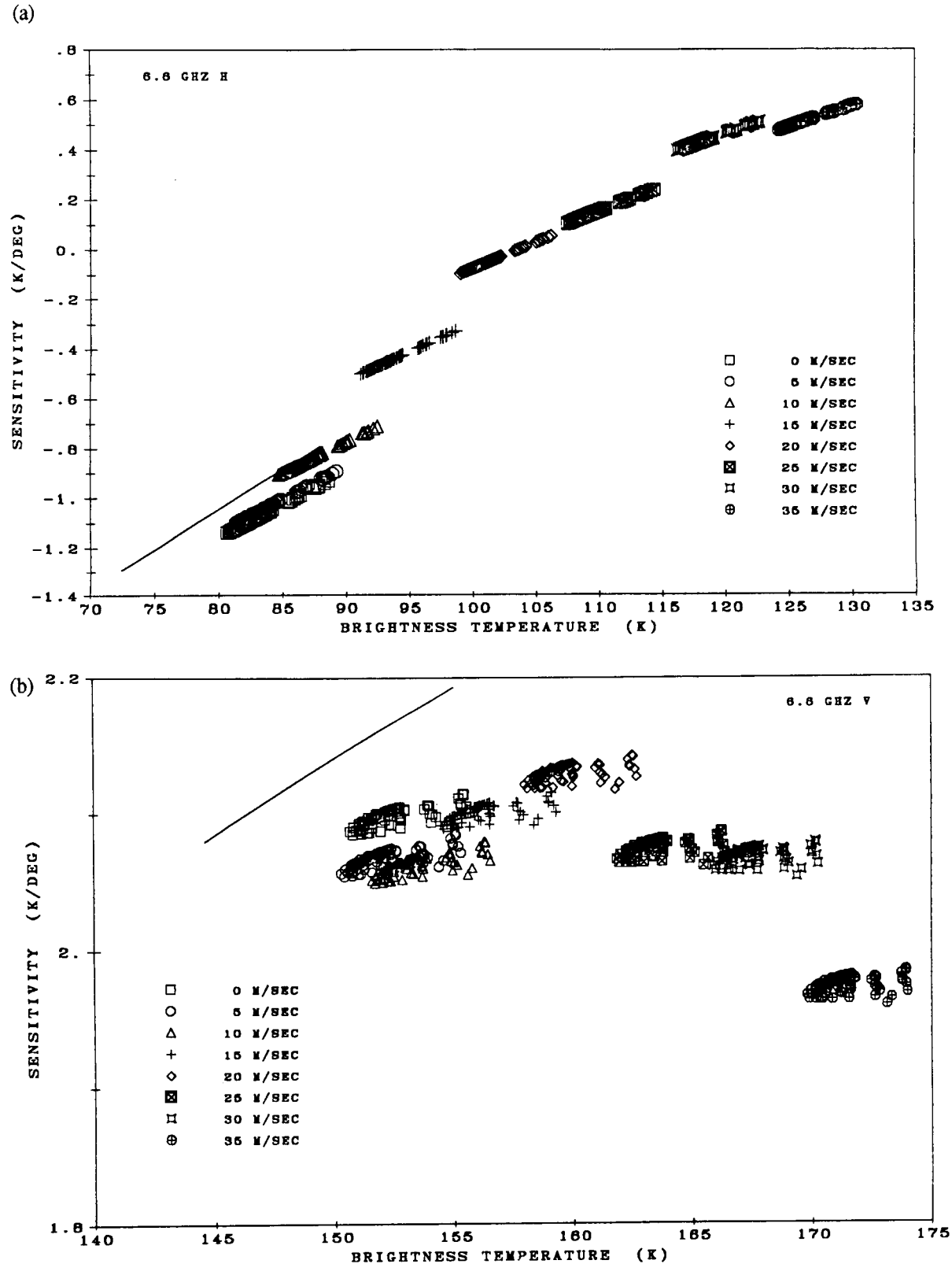

Figure 3.12 Sensitivity of the 6.6 GHz horizontal radiance (a) and vertical radiance (b) to a one-degree incident angle increase using the radiance model of Chang and Wilheit (1979). At each windspeed, the model was run for 81 different combinations of nine atmosphere types and nine cloud models. The solid line is the isothermal-atmosphere, smooth-surface case.

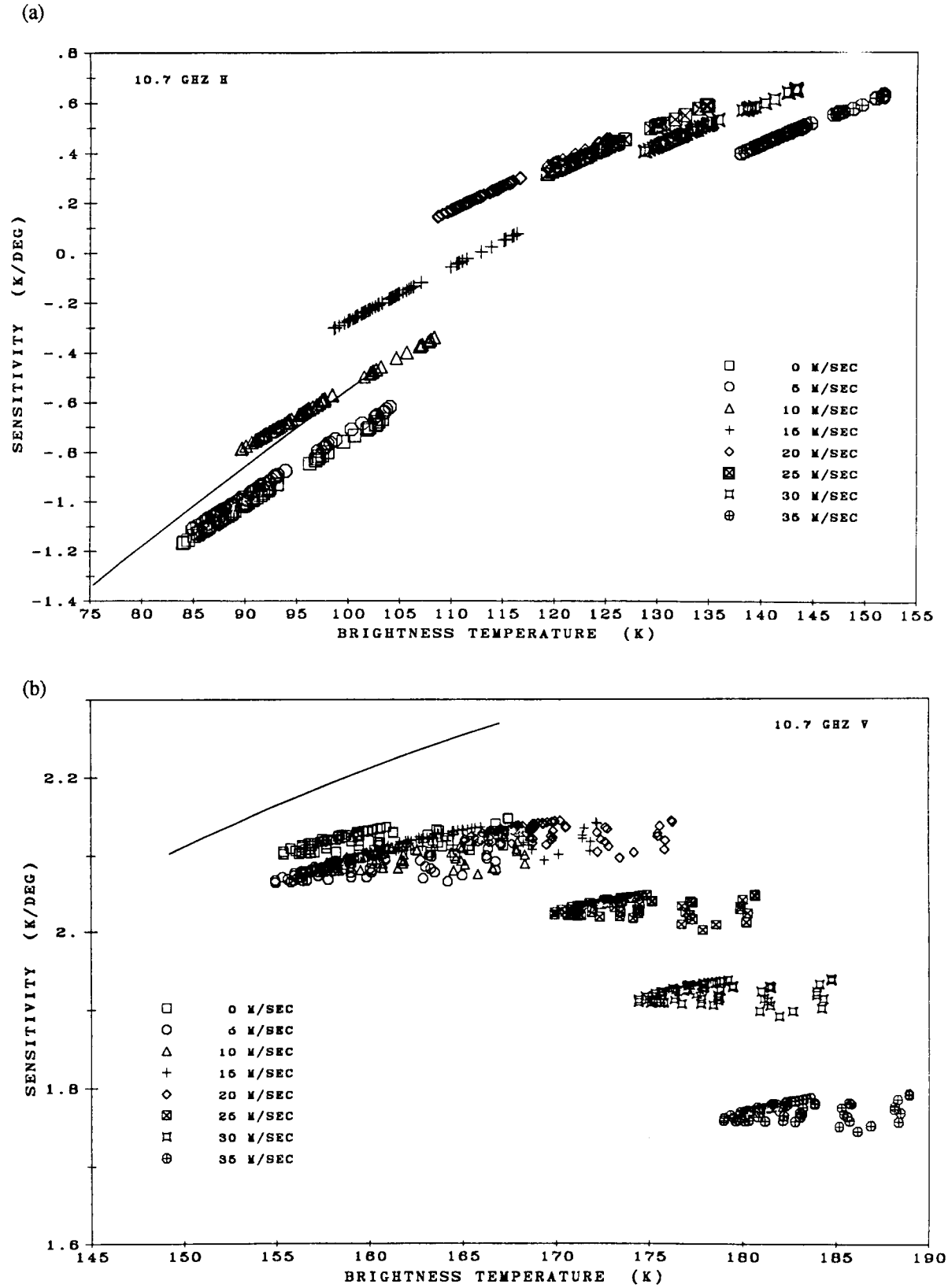

Figure 3.13 Sensitivity of the 10.7 GHz horizontal radiance (a) and vertical radiance (b) to a one-degree incident angle increase using the radiance model of Chang and Wilheit (1979). At each windspeed, the model was run for 81 different combinations of nine atmosphere types and nine cloud models. The solid line is the isothermal-atmosphere, smooth-surface case.

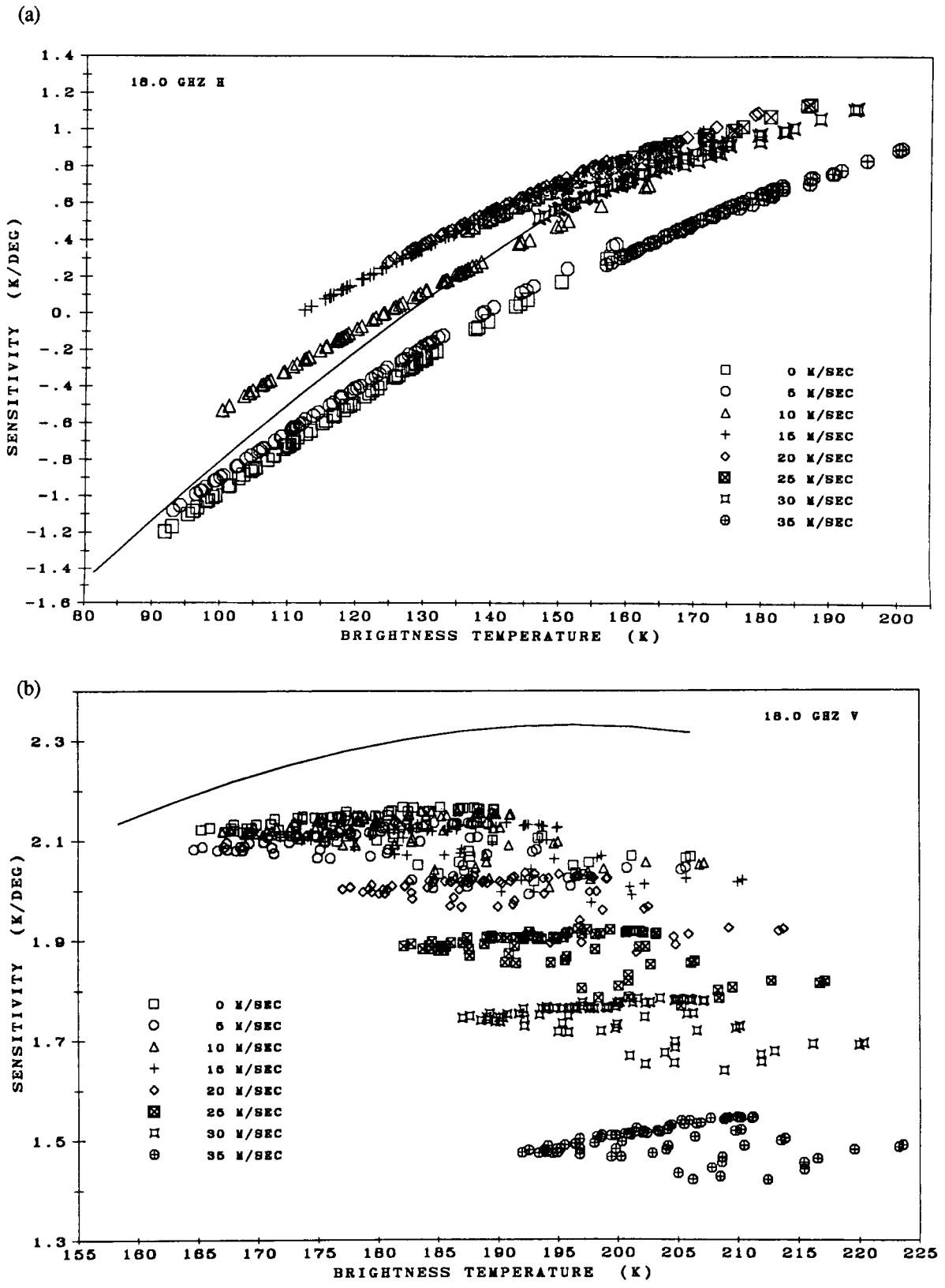

Figure 3.14 Sensitivity of the 18.0 GHz horizontal radiance (a) and vertical radiance (b) to a one-degree incident angle increase using the radiance model of Chang and Wilheit (1979). At each windspeed, the model was run for 81 different combinations of nine atmosphere types and nine cloud models. The solid line is the isothermal-atmosphere, smooth-surface case.

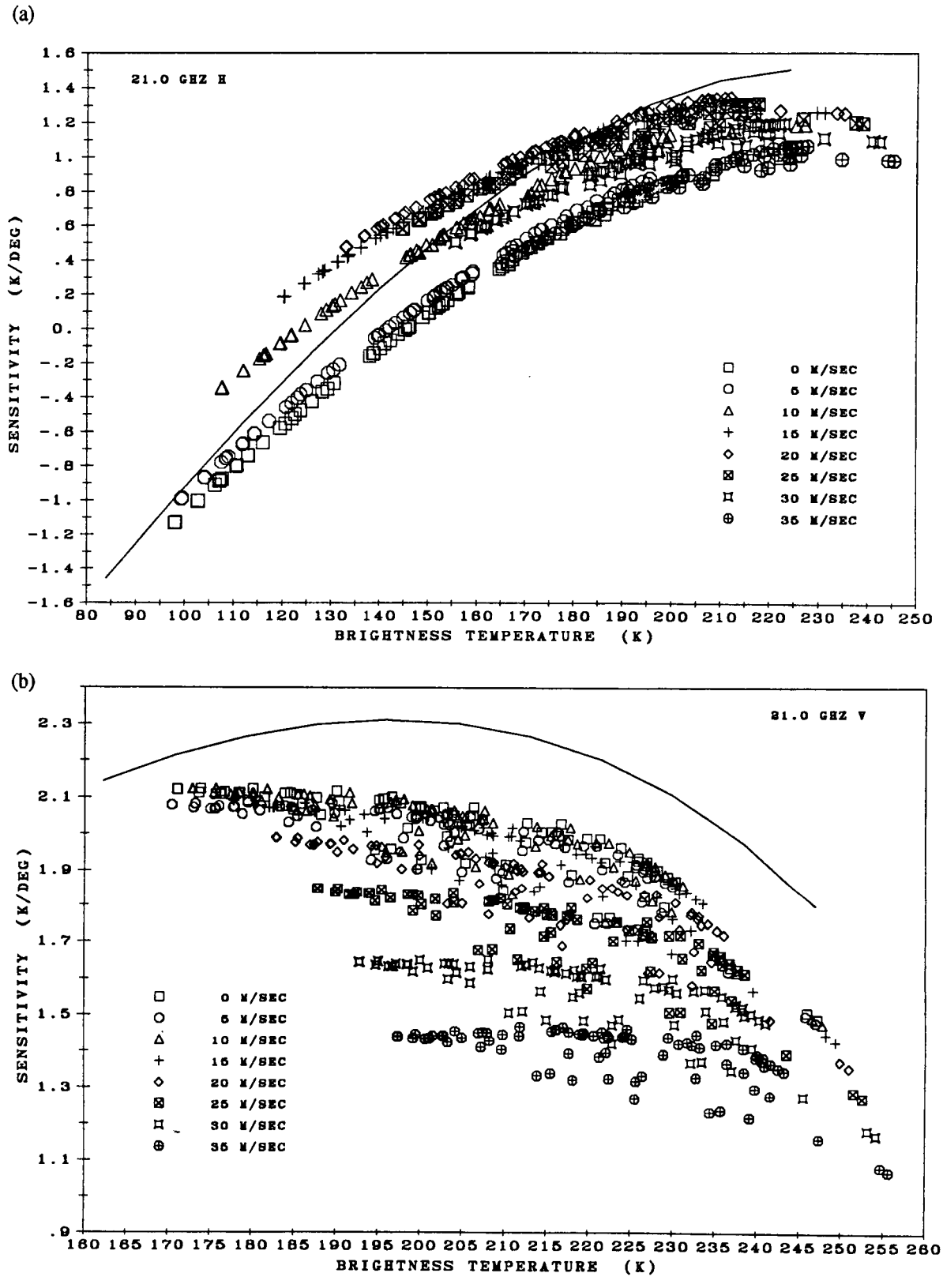

Figure 3.15 Sensitivity of the 21.0 GHz horizontal radiance (a) and vertical radiance (b) to a one-degree incident angle increase using the radiance model of Chang and Wilheit (1979). At each windspeed, the model was run for 81 different combinations of nine atmosphere types and nine cloud models. The solid line is the isothermal-atmosphere, smooth-surface case.

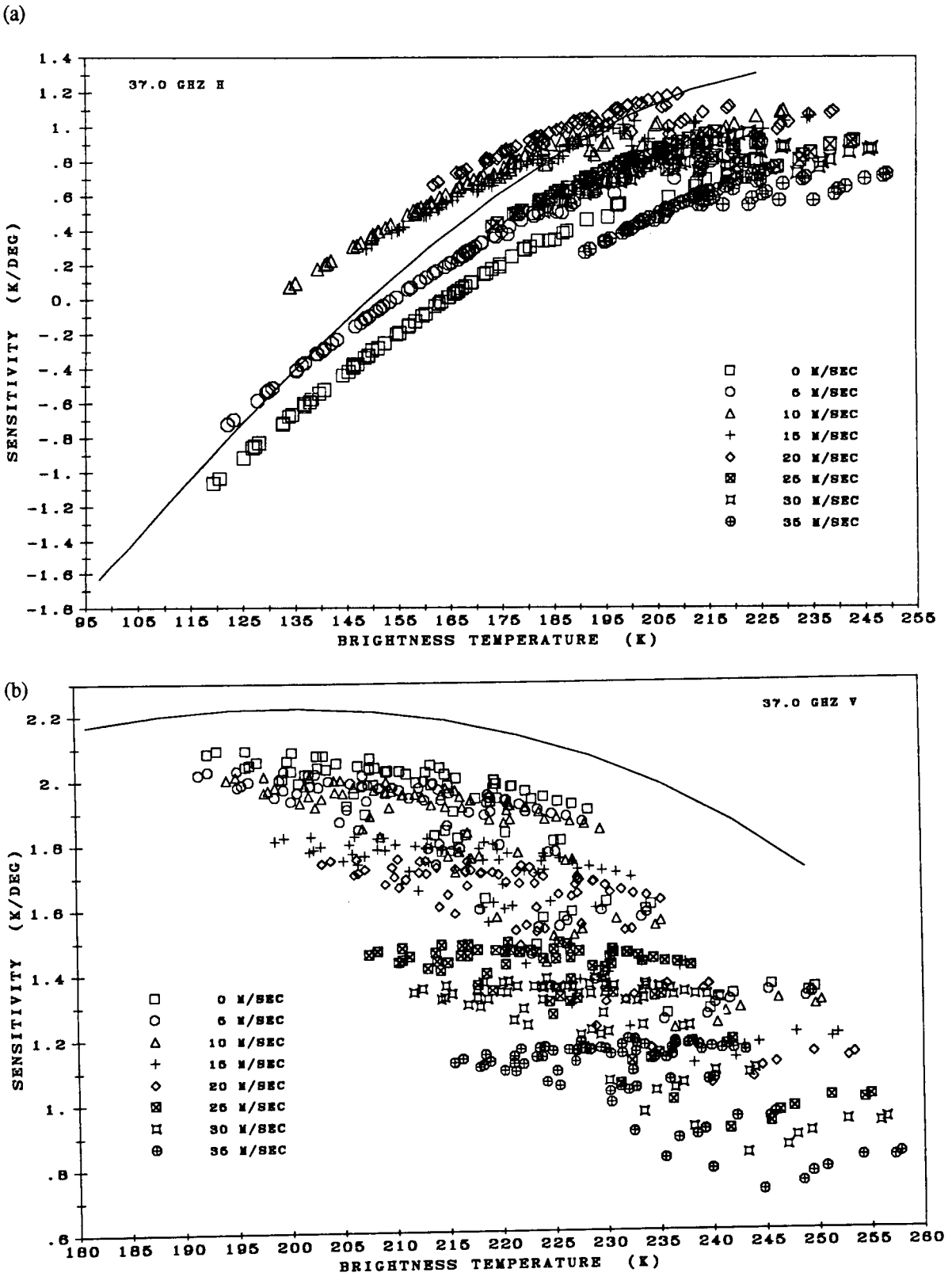

Figure 3.16 Sensitivity of the 37.0 GHz horizontal radiance (a) and vertical radiance (b) to a one-degree incident angle increase using the radiance model of Chang and Wilheit (1979). At each windspeed, the model was run for 81 different combinations of nine atmosphere types and nine cloud models. The solid line is the isothermal-atmosphere, smooth-surface case.

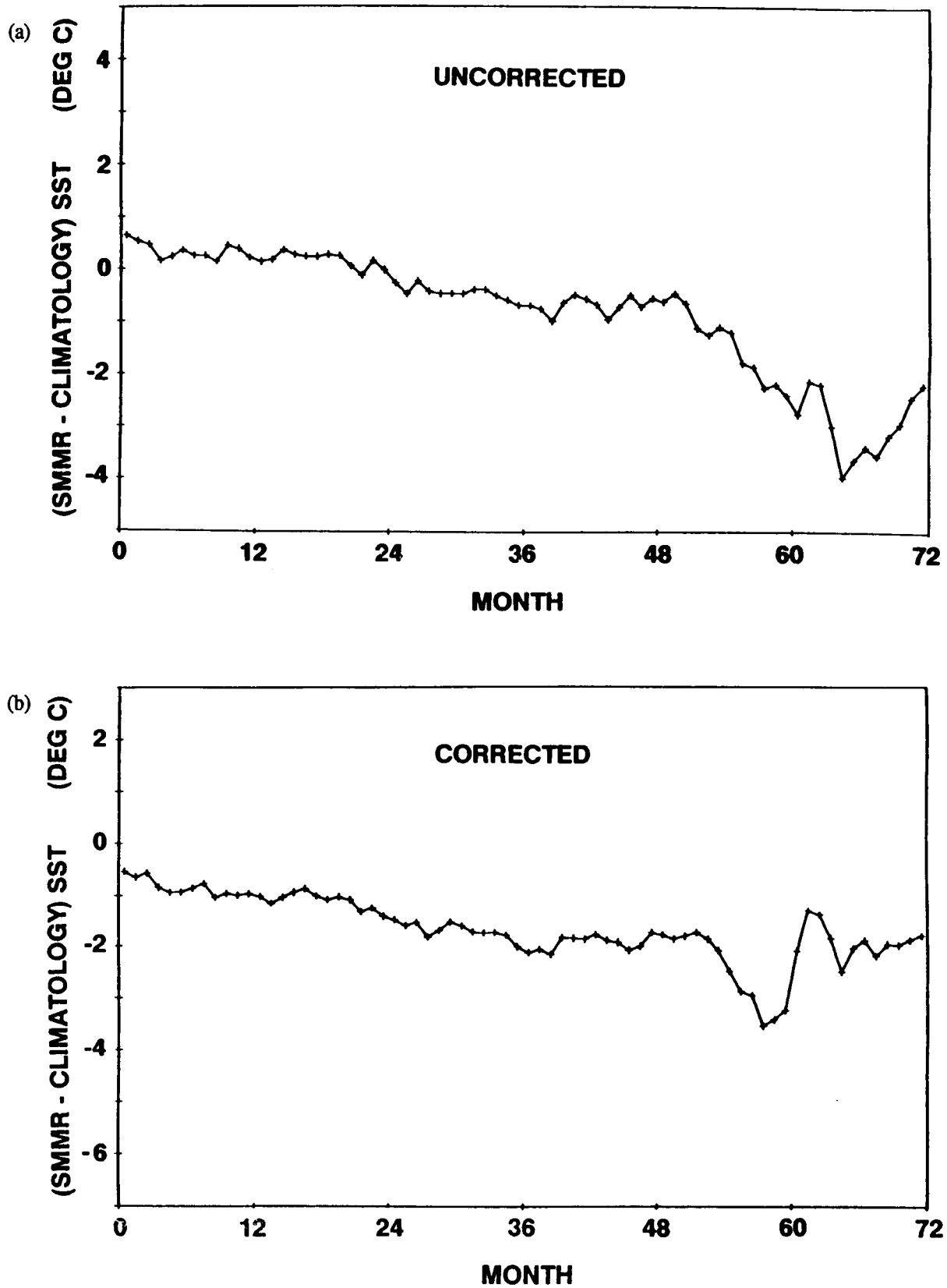

Figure 4.1 Monthly average difference between a climatological SST and SMMR retrieved SST (Version 1 algorithm) without (a) and with (b) the incident angle correction given by Equation (19).

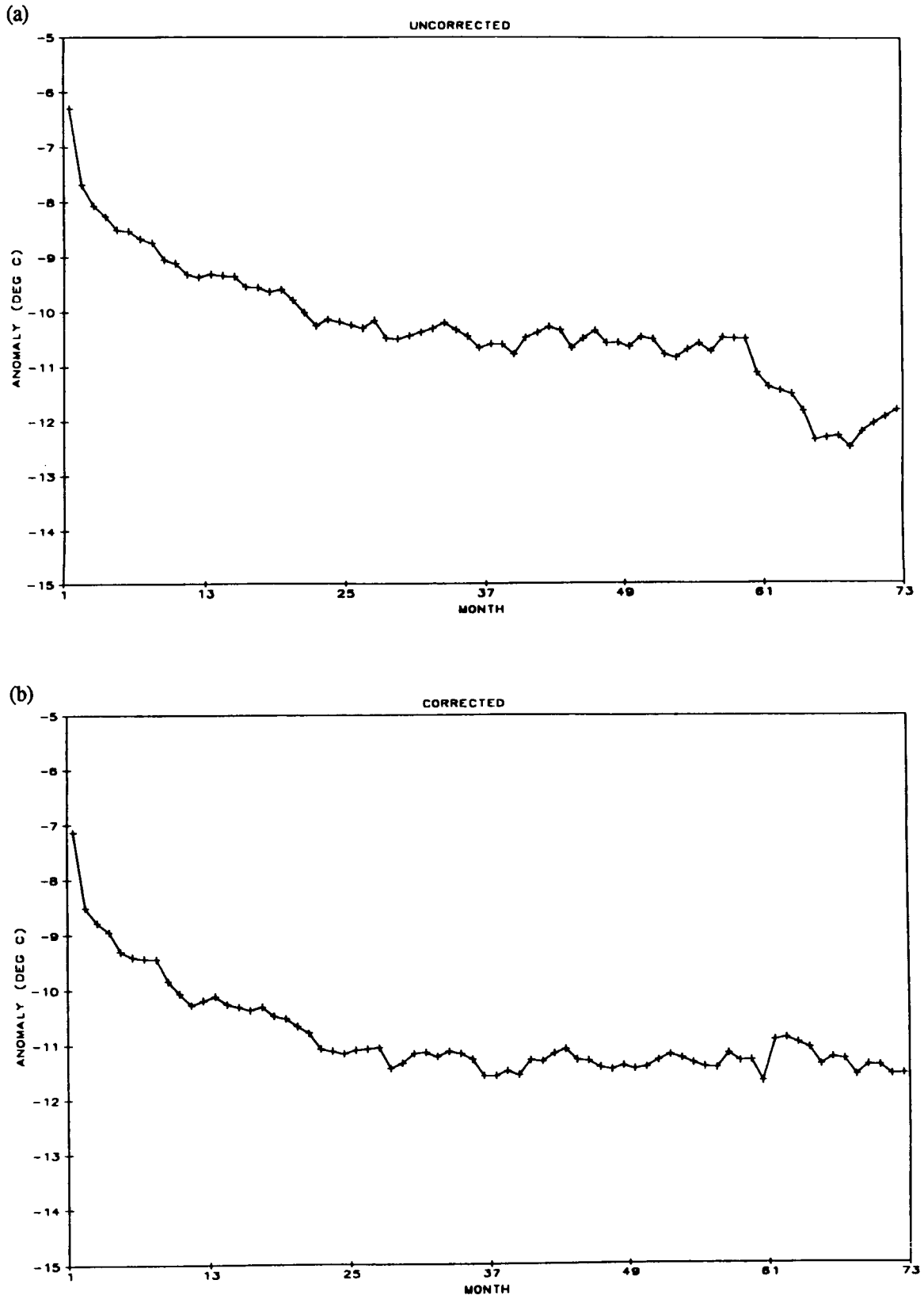

Figure 4.2 Monthly average difference between a climatological SST and SMMR retrieved SST (Version 2 algorithm) without (a) and with (b) the incident angle correction given by Equation (19).

(a)

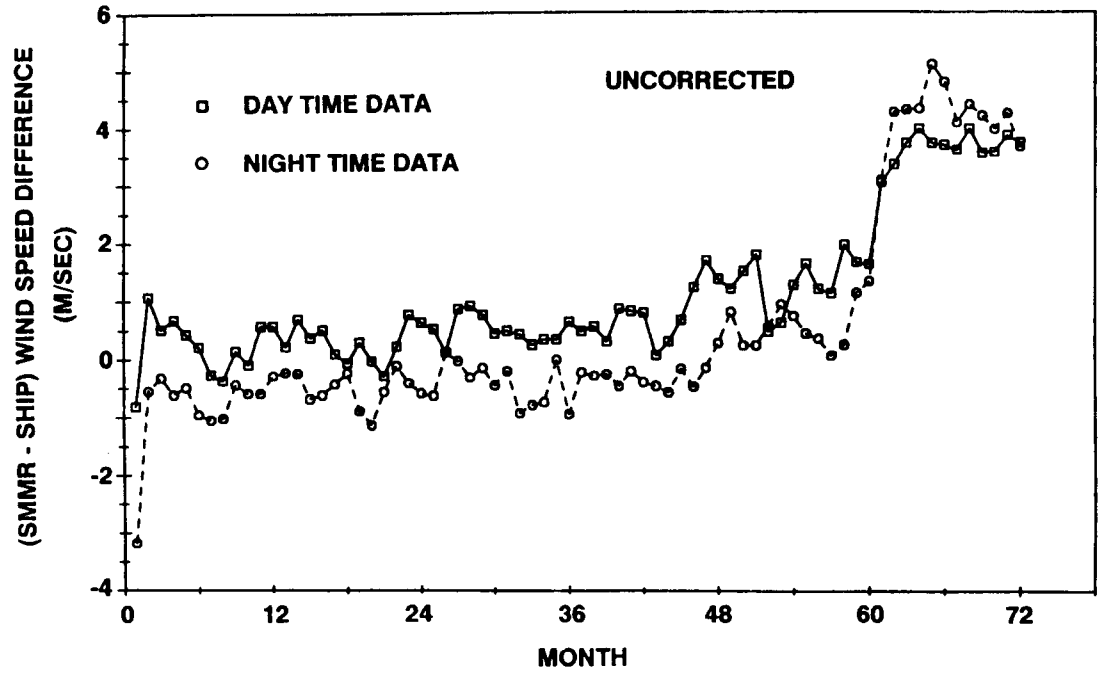

(b)

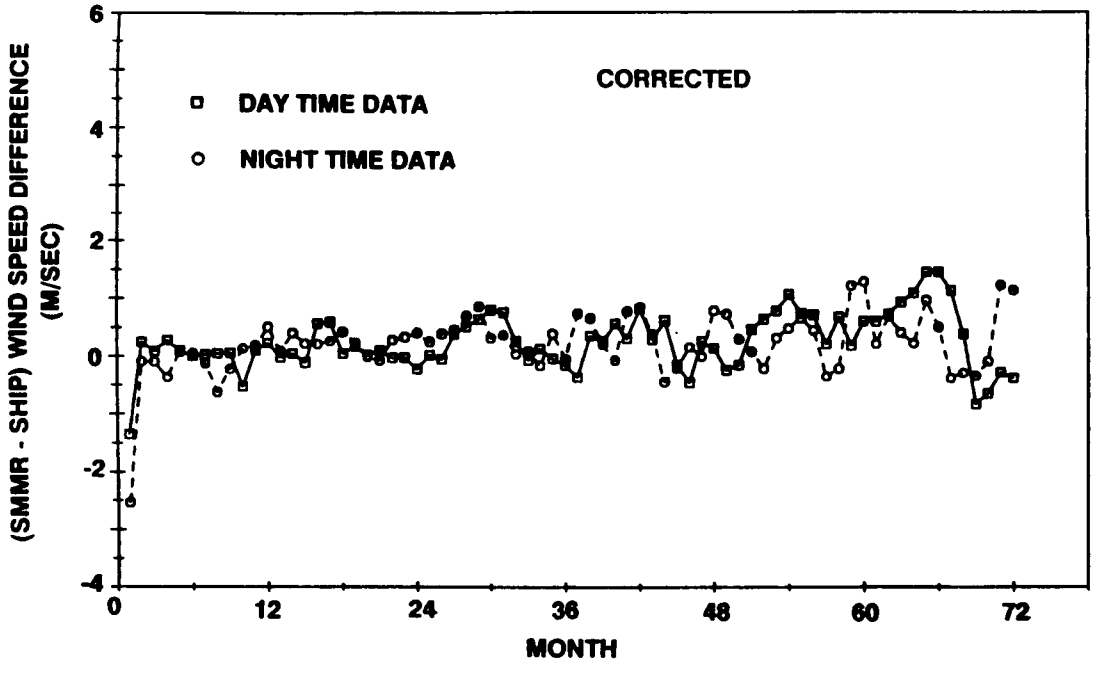

Figure 4.3 Monthly average difference between ship measured wind speeds and coincident SMMR retrieved wind speeds without (a) and with (b) the incident angle correction given by Equation (19).

NASA
National Aeronautics and Space Administration

Report Documentation Page

1. Report No.	2. Government Accession No.	3. Recipient's Catalog No.
NASA TM-4132		

4. Title and Subtitle
Attitude Angle Effects on Nimbus-7 Scanning Multichannel Microwave Radiometer Radiances and Geophysical Parameter Retrievals

5. Report Date
August 1989

6. Performing Organization Code
636

7. Author(s)
Daniel S. MacMillan and Daesoo Han

8. Performing Organization Report No.
89B00237

10. Work Unit No.

9. Performing Organization Name and Address
Goddard Space Flight Center
Space Data and Computing Division
Greenbelt, Maryland 20771

11. Contract or Grant No.
NAS5-29386

13. Type of Report and Period Covered
Technical Memorandum

12. Sponsoring Agency Name and Address
National Aeronautics and Space Administration
Washington, DC 20546-0001

14. Sponsoring Agency Code

15. Supplementary Notes
Daniel S. MacMillan: ST Systems Corporation (STX), Lanham, Maryland 20706
Daesoo Han: Goddard Space Flight Center, Greenbelt, Maryland 20771

16. Abstract
The attitude of the Nimbus-7 spacecraft has varied significantly over its lifetime. A summary of the orbital and long-term behavior of the attitude angles and the effects of attitude variations on Scanning Multichannel Microwave Radiometer (SMMR) brightness temperatures is presented. One of the principal effects of these variations is to change the incident angle at which the SMMR views the Earth's surface. The brightness temperatures depend upon the incident angle sensitivities of both the ocean surface emissivity and the atmospheric path length. Ocean surface emissivity is quite sensitive to incident angle variation near the SMMR incident angle, which is about 50 degrees. This sensitivity has been estimated theoretically for a smooth ocean surface and no atmosphere. A 1-degree increase in the angle of incidence produces a 2.9°C increase in the retrieved sea surface temperature and a 5.7 m/sec decrease in retrieved sea surface wind speed. An incident angle correction is applied to the SMMR radiances before using them in the geophysical parameter retrieval algorithms. The corrected retrieval data is compared with data obtained without applying the correction.

17. Key Words (Suggested by Author(s))
Scanning Multichannel Microwave Radiometer
SMMR
Microwave Remote Sensing
Nimbus 7 SMMR

18. Distribution Statement
Unclassified - Unlimited
Subject Category - 46

19. Security Classif. (of this report)	20. Security Classif. (of this page)	21. No. of pages	22. Price
Unclassified	Unclassified	52	A04